University of Zurich[UZH]

Stratospheric aerosol injection shifts permafrost drivers, accelerating thaw in the Eastern Arctic

ESS 510 Master's Thesis

Author
Isaline Businger
16-421-372

Supervised by
Prof. Dr. Gabriela Schaepman

Faculty representative
Prof. Dr. Gabriela Schaepman

30.04.2024
Department of Geography, University of Zurich

Abstract

The Arctic is experiencing accelerated warming, with a temperature increase rate four times higher than the global average, known as Arctic amplification. Permafrost, a global climate tipping point, poses significant concern as crossing its threshold could induce substantial and potentially irreversible changes in the Earth's climate system. Despite the growing interest in Stratospheric Aerosol Injection (SAI) as a potential climate change mitigation strategy, there exists a notable research gap in comprehending the relevance of various mechanisms driving seasonal permafrost variability under SAI scenarios. G6sulfur, a component of the Tier 1 GeoMIP6 experiments (Geoengineering Model Intercomparison Project), achieves a reduction in radiative forcing from SSP5-8.5 to SSP2-4.5 levels by introducing stratospheric aerosols along a single longitude band from 10°S to 10°N. G6sulfur induces significant alterations in large-scale atmospheric patterns, affecting zonal and meridional winds, cloud water and ice content, and the North Atlantic Oscillation (NAO) in both winter and summer, thereby influencing temperature variations as well as the reflection and absorption of longwave radiation. These changes result in an important shift in relative importance of summer permafrost thaw drivers in the high latitude Eastern Hemisphere, while maintaining nearly identical relative importance in the Western Hemisphere compared to SSP2-4.5. This, in return, leads to a faster decline in total high latitude permafrost area (-1.12×10^6 km$^2 \pm 0.57$, *P*-value < 0.0001) observed during the period 2080-2099 under G6sulfur. The reduction in total permafrost area is accompanied by an increase in summer thaw depth over the Eastern Hemisphere ($+0.50$ m ± 0.05, *P*-value < 0.0001), contrasting with a decrease over the Western Hemisphere (-0.15 m ± 0.03, *P*-value < 0.001). While G6sulfur as an SAI strategy shows promise in aligning with the radiative forcing goals of SSP2-4.5 and consequently slowing down the decline of permafrost, its implementation reveals potential spatial shifts in the importance of permafrost thaw drivers, underscoring the necessity for further optimizing the injection strategy to mitigate unintended consequences.

Table of Contents

List of Figures

List of Tables

1 Introduction

The definition of permafrost, as adopted by the International Permafrost Association, refers to the ground (i.e., soil and rock) that remains at or below 0°C for a period of minimum two years (ACGR, 1988). In the Northern Hemisphere, the region where permafrost could be expected represents 19 to 25% of the Earth's exposed land surface, which corresponds to an area of 18.7 to 24.3 x 10^6 km^2 (Gruber, 2012). Its considerable presence in high latitudes not only makes it a key component of the Arctic system but also positions it as a crucial carbon storage, given the substantial amount of carbon stored within these frozen grounds. Hugelius et al. (2014) estimated the northern circumpolar permafrost region to store 1035 Pg of soil organic carbon within the top 3 meters of the surface. As an illustration, Strauss et al. (2017) showed that the carbon stored in permafrost soils is even slightly more than the carbon contained in the atmosphere and furthermore, that it is accounting for roughly half of the carbon found in global soils.

The Arctic is undergoing accelerated warming, experiencing a rate of temperature increase four times faster than the global average, a phenomenon known as Arctic amplification (Rantanen et al., 2022). This rapid warming has profound consequences for the Arctic system, presenting a significant risk of thawing to a substantial portion of the cryosphere, including the permafrost (Biskaborn et al., 2019). As the permafrost thaws, the carbon it contains is released in the form of carbon dioxide (CO_2) and methane (CH_4) into the atmosphere, hence undergoing a transformative shift, transitioning from being a carbon sink to becoming a carbon source. CO_2 and CH_4, both being major greenhouse gases, further contribute to the warming effect in a positive climate feedback loop: the initial change, temperature increase, causes a secondary change, permafrost thaw and carbon release, that increases temperature and hence intensifies the initial change.

The impacts of this process on Arctic permafrost are concerning, with the CMIP6 models projecting that for every 1°C increase in the global mean surface air temperature, the annual mean frozen volume in the top 2 meters of the soil is projected to decrease by approximately 10 to 40% (Burke et al., 2020). At this rate, it has even been shown that under a RCP8.5 scenario, the permafrost in the northern latitudes would likely act as a source of carbon to the atmosphere at the end of the 21st century (McGuire et al., 2018). The degradation of the near-surface permafrost under a business-as-usual scenario would create an additional forcing of 0.14 W/m^2 by 2100, and 0.35 W/m^2 by 2200, resulting in an additional warming of 0.1°C, respectively 0.38°C (Schneider Von Deimling et al., 2012).

In addition to the degradation of frozen grounds in high latitudes, permafrost is also of special concern as it is a global climate tipping point, where if the threshold is crossed, can cause substantial and, potentially, irreversible changes in the Earth's climate system. McKay et al. (2022) showed that the collapse of boreal permafrost would occur at an estimated global warming threshold of 4°C relative to pre-industrial and cause a global-mean surface temperature feedback of about +0.2 to +0.4°C.

The importance of Arctic permafrost and its concerning thaw make it essential to act urgently. However, due to the inherently slow implementation process of CO_2 emission reduction, the use of this sole solution may not be enough to prevent further impacts of climate change. In this regard, several geoengineering methods have been proposed as an additional solution alongside mitigating emissions, also often considered as measures to buy time. Stratospheric aerosol injection (SAI) is a solar radiation management method that mimics the real-world process of volcanic eruptions by injecting sulphate aerosols in the stratosphere. This aims to reflect some of the shortwave radiation from the sun back into space and results in cooling the earth (Jiang et al., 2019). This design has gained considerable attention in the literature, suggesting it as a potentially advanced geoengineering method in terms of research. Considering this, and the almost non-existent policies on the matter, it seems likely that SAI might be one of the first geoengineering methods to be implemented. Planned small-scale outdoor experiments of SAI, such as the SCoPEX project by Harvard University (*SCoPEX*, n.d.), have halted, while Make Sunsets, a private company, has been able to conduct such experiments and continues to sell carbon credits (*Make Sunsets*, n.d.). It is therefore urgent to conduct assessments of SAI and evaluate its efficiency and impacts to be able to provide policy and decision makers with essential scientific knowledge.

In that context, the Geoengineering Model Intercomparison Project (GeoMIP) was created as a coordinating framework with the main aim being to answer the question "What are the expected climate effects of geoengineering?" (*The Geoengineering Model Intercomparison Project (GeoMIP)*, n.d.). GeoMIP is one among 20 other model intercomparison projects, called MIPs, within the Coupled Model Intercomparison Project (CMIP). CMIP is one of the flagship efforts of the World Climate Research Programme (WCRP). Since its creation in 2010, GeoMIP offered 18 different standardized climate model experiments for understanding processes and impacts of solar geoengineering methods. The hope is to provide consistency among geoengineering studies and hence facilitate the comparison of observations between models (Visioni et al., 2023).

To date, only three studies investigating the response of permafrost under SAI were made using the GeoMIP framework. Chen et al. (2020) studied permafrost carbon-climate feedbacks under the GeoMIP G4 experiment which is a scenario injecting 5 Tg of SO_2 per year into the lower stratosphere located above the equator. Chen et al. (2023) analysed the response of permafrost, its active layer, and the related response of soil organic carbon under the GeoMIP G6solar and G6sulfur experiments which are scenarios reducing the forcing from SSP5-8.5 to SSP2-4.5 using respectively, solar irradiance reduction and injections of stratospheric sulphate aerosols. The outputs of GeoMIP G6solar and G6sulfur experiments were also used by Liu et al. (2023), within the data-constrained and process-based PInc-PanTher model of permafrost carbon storage, to investigate the impacts of G6solar and G6sulfur on permafrost area and soil carbon loss. Outside of the GeoMIP framework, four other studies were done relating SAI to permafrost: Jiang et al. (2019) used simulations of the Stratospheric Aerosol Geoengineering Large Ensemble (GLENS) to study the seasonal cycle of climate change, including its impact on permafrost area, H. Lee et al. (2019) worked with the Norwegian Earth System Model (NorESM) to investigate the effects of SAI on permafrost temperature and near-surface permafrost area, W. R. Lee et al. (2023) ran the Community Earth System Model (CESM) to examine the possibility of SAI in preserving the Arctic, including the permafrost, and Müller et al. (2024) utilized the Norwegian Earth System Model (NorESM1) to investigate the effect of various geoengineering methods, including stratospheric aerosol injection, on Arctic temperatures and their consequent impact on Arctic system dynamics, such as permafrost.

Permafrost freeze-thaw dynamics are subject to complex and very interconnected processes, which can be spatially and temporarily separated from the stratospheric aerosol injection. These mechanisms encompass the following external forcings: short- and longwave fluxes (including change in surface albedo and cloud cover), sensible and latent heat fluxes (including air temperature and humidity), ground heat flux (including thermal properties), precipitation (rain and snow), surface cover with vegetation, snow, and ponds as well as wind (Van Huissteden, 2020).

Besides incoming solar radiation, snow cover and vegetation dynamics are key drivers influencing the thermal regime of permafrost. On one side, snow acts as an insulating layer, reducing heat transfer between the ground and the atmosphere (Stieglitz et al., 2003). Therefore, changes in snow cover duration, depth, and density can alter the energy budget at the land surface, affecting the thermal stability of permafrost. On the other side, vegetation type has been shown to act as an important predictor for components of the surface energy budget during the Arctic summer (Oehri et al., 2022) and to influence soil moisture dynamics through

evapotranspiration (Ohta et al., 2008). In addition, vegetation changes, such as shifts in species composition, can influence the exchange of energy and water between the land surface and the atmosphere (Eugster et al., 2000).

Furthermore, snow and vegetation have a direct influence on the albedo of a surface, leading to variations in energy fluxes and subsequently impacting permafrost thermal dynamics. Snow accumulation and its properties exhibit seasonal and year-to-year variations, hence leading to changes in albedo: as snow ages, its albedo decreases compared to fresh snow (Gallet et al., 2011) and in the Arctic, the albedo effect is most prominent during spring when the snowpack persists while the sun angle rises (Sturm, 2005). Vegetation cover significantly affects the albedo as well, with boreal forests having a lower albedo compared to shorter vegetation. Similarly, variations in albedo are observed within tundra environments, where dry tundra vegetation, including lichen-rich and shrub vegetation, tends to have a higher albedo than wet tundra with moist soil or standing water between the vegetation. These differences in albedo can have notable impacts on the incoming shortwave radiation and, consequently, the energy budget within these ecosystems (Eugster et al., 2000).

According to the research conducted by H. Lee et al. (2019), in a SAI scenario, there is a reduction in rain and an increase in snow in high latitude regions (55–85°N). Chen et al. (2023) reported similar findings, indicating a decrease in summer precipitation and an increase in winter precipitation in the northern latitudes under SAI. Concerning the ability of SAI to preserve permafrost, it has been shown that this geoengineering method can slow down the decrease of permafrost area but not stabilize it (Chen et al., 2023; H. Lee et al., 2019). The interplay between vegetation, snow cover, and permafrost dynamics is complex and varies spatially and temporally. Given this complexity and interconnectivity, it is plausible to assume that the aerosols used for implementing SAI may interfere with these processes. This interference could potentially lead to seasonally opposing effects that influence the energy budget of permafrost and therefore impact the efficiency of SAI in effectively preserving permafrost.

The relative contributions of these different processes by which stratospheric aerosol injection impacts permafrost are not yet fully understood and may also depend on the respective injection strategy. In this context, understanding the response of the different mechanisms to changes in radiative forcing induced by solar geoengineering scenarios becomes crucial.

Despite the growing interest in SAI as a potential strategy to mitigate the impacts of climate change, there is a significant research gap in understanding the relevance of the different

mechanisms driving seasonal permafrost variability under SAI scenarios. While several studies have examined the impacts of SAI on permafrost, there is limited knowledge regarding the importance of specific drivers and their seasonal variations. Understanding the constraints and the point of diminishing returns is crucial for developing realistic and effective SAI strategies. Our study therefore aims to understand to which extent stratospheric sulphate aerosol injection, as implemented in the GeoMIP G6sulfur scenario, causes a shift in key drivers influencing permafrost freeze-thaw dynamics.

2 Methods

To investigate the impacts of SAI strategies on permafrost and associated underlying processes, our study utilizes output data from models participating in GeoMIP Phase 6, the latest release proposed in 2015. Specifically, we focus on analyzing the G6sulfur and G6solar scenarios simulated by six coupled Earth System Models (see Table 1).

G6sulfur reduces the forcing from a ScenarioMIP Tier 1 high forcing scenario (SSP5-8.5) to a ScenarioMIP Tier 1 medium forcing scenario (SSP2-4.5) through stratospheric aerosol or aerosol precursor injections, with the decadal means being in the range of ±0.1 Wm^{-2}. The aerosol injections are concentrated along a specific line positioned at the 0° longitude band between latitudes 10°S and 10°N, spanning between 18 km and 20 km across the atmospheric model layers. On the other hand, G6solar is identical to G6sulfur but simulates SAI by directly reducing solar irradiance instead of utilizing SO_2 injections. The simulations for both scenarios run from 2020 to 2100 (Kravitz et al., 2015).

G6sulfur and G6solar were thought to be used in parallel to enable the comparison between the impacts of stratospheric aerosol injections and solar irradiance reduction. As the spatial distribution of forcing is expected to have less differences among models using G6solar compared to those using G6sulfur, it allows to determine the uncertainties associated with the transport of stratospheric sulphate aerosols (Visioni et al., 2023). Since the two geoengineering scenarios aim to reduce the forcing to match that of the SSP2-4.5 scenario, the SSP2-4.5 scenario is selected as the control, providing a basis for comparison and analysis across different experimental approaches. The statistical analysis employed for assessing differences between the geoengineering and control scenarios involved using the two-sample Welch's t-test.

Table 1: Overview of the six Earth System Models (ESMs) used in this study (adapted from Visioni et al. (2021). (a) Tilmes et al. (2015), (b) Niemeier & Schmidt (2017). For some models there are more ensemble members of the SSP2-4.5 experiments available than for G6solar and G6sulfur, all of them were used in this study. (c) For the UKESM1-0-LL there were different numbers of ensemble members for the SSP2-4.5 among different variables. The maximum number of ensemble members of each variable was used. All models feature interactive marine biogeochemistry and are coupled with an interactive land model.

Model Name	Reference(s)	G6solar	G6sulfur	ssp245	Stratospheric Aerosol	Soil layers	Soil depth (m)
		number of simulations			in G6sulfur		
CESM2-WACCM	Danabasoglu et al.(2020)	2	2	5	SO2 injection	25	42.0
CNRM-ESM2-1	Gettelman et al. (2019) Séférian et al. (2019)	1	3	10	AOD scaled (a)	14	10.0
IPSL-CM6A-LR	Boucher et al. (2020)	1	1	11	SO2 injection	18	65.6
MPI-ESM1-2-HR	Lurton et al. (2020) Muller et al. (2018)	3	3	2	AOD scaled (b)	5	7.0
MPI-ESM1-2-LR	Muller et al. (2018)	3	3	50	AOD scaled (b)	5	7.0
UKESM1-0-LL	Sellar et al. (2019)	3	3	6-19 (c)	SO2 injection	4	2.0

We investigated the permafrost area, summer permafrost thaw depth, and various permafrost drivers, including atmospheric, energy flux, precipitation, soil, and vegetation variables (see Table 2). The ensemble means from each scenarios' ensemble members are computed per model and then bilinearly regridded to a shared resolution of 0.5° x 0.5° using the Climate Data Operator Version 2.3.0 from the Max Planck Institute. The results represent multi-model means across the six Earth System Models (ESMs). Atmospheric 3D variables are vertically interpolated to standard hectopascal (hPa) levels.

Changes in summer permafrost thaw depth and the different predictor variables for experiments G6solar and G6sulfur are analysed relative to SSP2-4.5 within a defined geographical area characterized by a permafrost probability exceeding 50% based on mean annual air temperature (MAAT) projections for the end of the 21st century (2080-2099). To define this region of interest, we apply an observation-based relationship between mean annual air temperature (MAAT) and permafrost probability, as initially established by Gruber (2012) and refined in the methodology outlined by Chadburn et al. (2017). The relationship is represented by the equation $F_{MAAT} = \frac{1}{2} erfc\left(\frac{MAAT+\mu}{\sqrt{2\sigma^2}}\right)$, where mean $\mu = 4.38$ °C, standard deviation $\sigma = 2.59$ °C, and erfc() returns the complementary error function. We assume that any grid cell with observed permafrost probability of 50% or higher should be recognized by the models as containing permafrost (Burke et al., 2020). Additionally, we apply a filter to include only grid cells with a land fraction above 35%.

The depth of thawing from the surface is determined by using monthly mean soil temperatures at various depths. Soil temperature data is interpolated between each model layer to estimate temperatures at specific depths. The thaw depth is then defined as the depth at which the temperature crosses 0°C (Burke et al., 2020). It is important to note that certain models may exhibit poorly resolved soil temperature profiles, which could introduce biases into the estimates (Chadburn et al., 2015).

We conducted a variance partitioning analysis (adapted from Oehri et al., 2022) to assess the ability of 18 selected factors (see Table 2), driving the complex process of permafrost thawing and freezing, to predict the magnitude of summer permafrost thaw depth (SPTD). This method helps mitigate statistical confounding of predictors by distinguishing the variance in SPTD that can be explained jointly or independently by various drivers. To accomplish this, we used a set of 18 selected predictors related to SPTD to construct all possible models comprising three predictors each. For every model, we evaluated the variance explained by individual predictors within a triplet of predictors when placed first, when placed last, and when averaged across all possible orderings in the models. Subsequently, we computed the average explained variance (%) for each SPTD predictor across all models for each SPTD variable. This process involved testing 680 unique SPTD predictor triplets across 6 different predictor orders, resulting in a total of 4080 models. We conducted this analysis in two distinct northern high-latitude regions: the Western Hemisphere (longitude 180° - 360°) and the Eastern Hemisphere (longitude 0°-180°), and during two different seasons: winter (DJF: December, January, February) and summer (JJA: June, July, August), using means over the period 2080-2099.

For every 3D variable (see Fig. S1-S8 in Supplements), encompassing latitude/longitude, time, and pressure levels (clw: mass fraction of cloud liquid water, cli: mass fraction of cloud ice, ua: eastward wind, and va: northward wind), individual variance partitioning analyses were conducted for each region and season. The objective was to ascertain the predictive power of the different pressure levels of each 3D variable in explaining variations in SPTD. The specific pressure level demonstrating the most predictive power was chosen for integration into the variance partitioning analysis alongside the other 2-dimensional variables (latitude/longitude and time). The variance partitioning analysis and the correlation maps of SPTD drivers were conducted in R version 4.1.3.

The North Atlantic Oscillation (NAO) was assessed through the pressure difference between Iceland and the Azores, as per the methodology outlined by Jones et al. (2021). We utilized the monthly mean sea-level pressure (MSLP) data from 2080 to 2099 from the nearest model grid

cells to Stykkishólmur, Iceland (65°05'N, 22°44'W), and Ponta Delgada in the Azores (37°44'N, 25°41'W). We derived a NAO-index by detrending the time series of MSLP at each location, normalizing the resulting anomalies by their standard deviation, and then calculating the difference of the normalized anomalies between G6sulfur and SSP2-4.5. The 3-month rolling mean of the NAO-index was correlated with the normalized 3-month rolling mean temperature, as well as the mass fraction of cloud liquid water and ice, along 18 geographical segments spanning from 0°E to 180°E and ranging from 65°N to 75°N. Each of these segments cover an area of 10° longitude and 10° latitude.

Table 2: Overview of the variables used in the six ESMs specified by long name, abbreviation, units, and dimensions being either 2 dimensional (latitude / longitude) or 3 dimensional (latitude / longitude and height in pressure levels (hPa) or depths (m)).

Variable Name	Variable ID	Units	Dimensions	Variable Name	Variable ID	Units	Dimensions
Air Temperature	tas	K	2D	Surface Downwelling Shortwave Flux in Air	rsds	W m-2	2D
Near Surface Relative Humidity	hurs	%	2D	Surface Upwelling Shortwave Flux in Air	rsus	W m-2	2D
Sea Level Air Pressure	psl	hPa	2D	Surface Downwelling Longwave Flux in Air	rlds	W m-2	2D
Near Surface Wind Speed	sfcWind	m s-1	2D	Surface Upwelling Longwave Flux in Air	rlus	W m-2	2D
Eastward Wind	ua	m s-1	3D	Surface Upward Sensible Heat Flux	hfss	W m-2	2D
Northward Wind	va	m s-1	3D	Surface upward latent heat flux	hfls	W m-2	2D
Cloud Cover	clt	%	2D	Moisture in Uper Portion of Soil Colum	mrsos	kg m-2	2D
Precipitation Flux	pr	kg m-2 s-1	2D	Leaf Area Index	lai	1	2D
Mass Fraction of Cloud Liquid Water	clw	kg kg-1	3D				
Mass Fraction of Cloud Ice	cli	kg kg-1	3D	Temperature of Soil	tsl	K	3D

3 Results

3.1 Evolution of permafrost area under geoengineering

At the start of the simulation in 2020, the permafrost area derived from the multi-model ensemble mean of MAAT is at 15.56 x 10^6 km^2 for SSP2-4.5, 15.49 x 10^6 km^2 for G6solar, and 14.84 x 10^6 km^2 for G6sulfur (Fig. 1a). These results closely align with recent studies summarized in Obu (2021), where the current estimated permafrost area in the Northern Hemisphere ranges between 12.2 and 17.7 x 10^6 km^2. Examining the period from 2030 to 2049, which is a decade into the simulation (green shaded in Fig. 1a), there are no statistically significant differences in the mean values between the geoengineering and control experiments (Fig. 1b). However, by the end of the simulation (2080-2099 period, blue shaded in Fig. 1a), permafrost area under G6solar and G6sulfur decreases more rapidly than SSP2-4.5, with statistically significant differences in the mean values (Fig. 1c). The observed difference is -0.39 ± 0.44 x 10^6 km^2 under G6solar, and -1.12 ± 0.57 x 10^6 km^2 under G6sulfur (Fig. 1c).

Figure 1d illustrates the permafrost area under SSP2-4.5, G6solar, and G6sulfur, respectively, comparing the periods of 2030-2049 in green and 2080-2099 in blue. The largest difference in permafrost area is observed in the Eastern Hemisphere, specifically between longitudes 90°E and 130°E, bordered by the Central Siberian Plateau to the east and the Verkhoyansk Range to the west. Within this geographic region, permafrost area is retreating faster under G6sulfur compared to G6solar and SSP2-4.5.

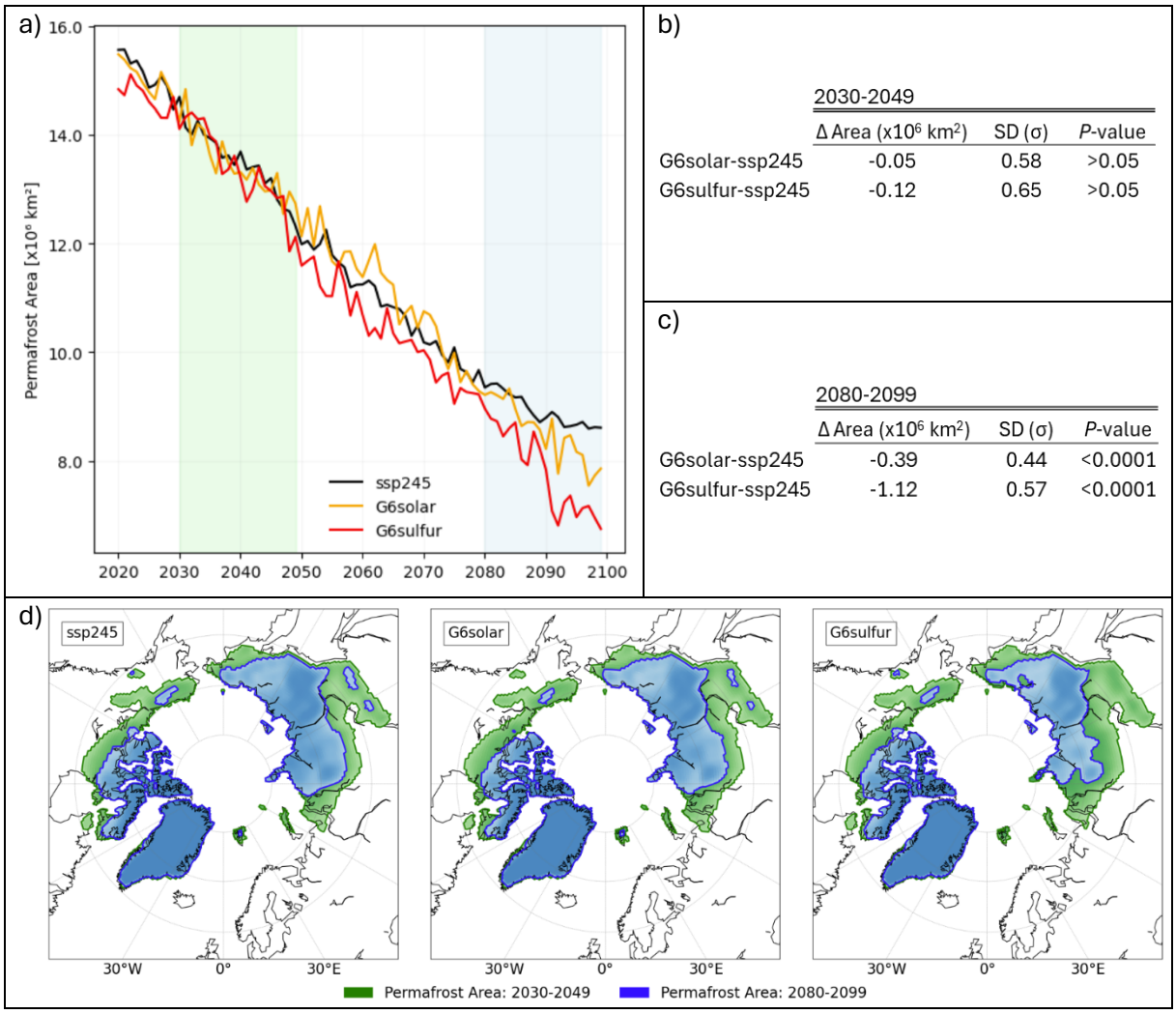

Fig. 1: Evolution of permafrost area under geoengineering. a) Yearly evolution of Permafrost Area (in 10^6 km^2 with $PF_{>50\%}$ MAAT based) b) Difference in mean Permafrost Area ($PF_{>50\%}$ MAAT based) over time period 2030-2049 and 2080-2099 for G6solar vs SSP2-4.5 c) Difference in mean Permafrost Area ($PF_{>50\%}$ MAAT based) over time period 2030-2049 and 2080-2099 for G6sulfur vs SSP2-4.5 d) Permafrost Extent ($PF_{>50\%}$ MAAT based) for the three simulations SSP2-4.5 G6solar, G6sulfur over the time period 2030-2049 (green) and 2080-2099 (blue).

3.2 Difference in thaw depth under geoengineering

When analysing changes in permafrost area under varying conditions, thaw depth - representing the extent of seasonal thawing above the permafrost - can be used to study how permafrost responds to geoengineering, as thaw depth directly influences permafrost stability (Garnello et al., 2021). Our analysis shows that both G6solar and G6sulfur result in deeper summer thaw depths at northern high latitudes compared to SSP2-4.5 (Fig. 2b). However, regionally, G6sulfur creates a statistically significant deeper summer thaw depth in the Eastern Hemisphere (+0.5 ± 0.05 m, *P*-value < 0.0001), whereas in the Western Hemisphere, it creates a statistically significant shallower summer thaw depth (-0.15 ± 0.03 m, *P*-value < 0.001). In the G6sulfur,

there is a spatial overlap between the increase and decrease of permafrost area (Fig. 1d) and the observed decrease and increase in summer thaw depth (Fig. 2a). These results confirm the findings of Chen et al. (2023), who, using the CLM5 model, observed similar spatial patterns in the permafrost area mapped from the annual maximum active layer thickness. Based on the observed spatial distributions and the significance of the difference, we direct our further investigations towards understanding the underlying processes driving the patterns of summer permafrost thaw depth in the Eastern and Western Hemisphere under G6sulfur.

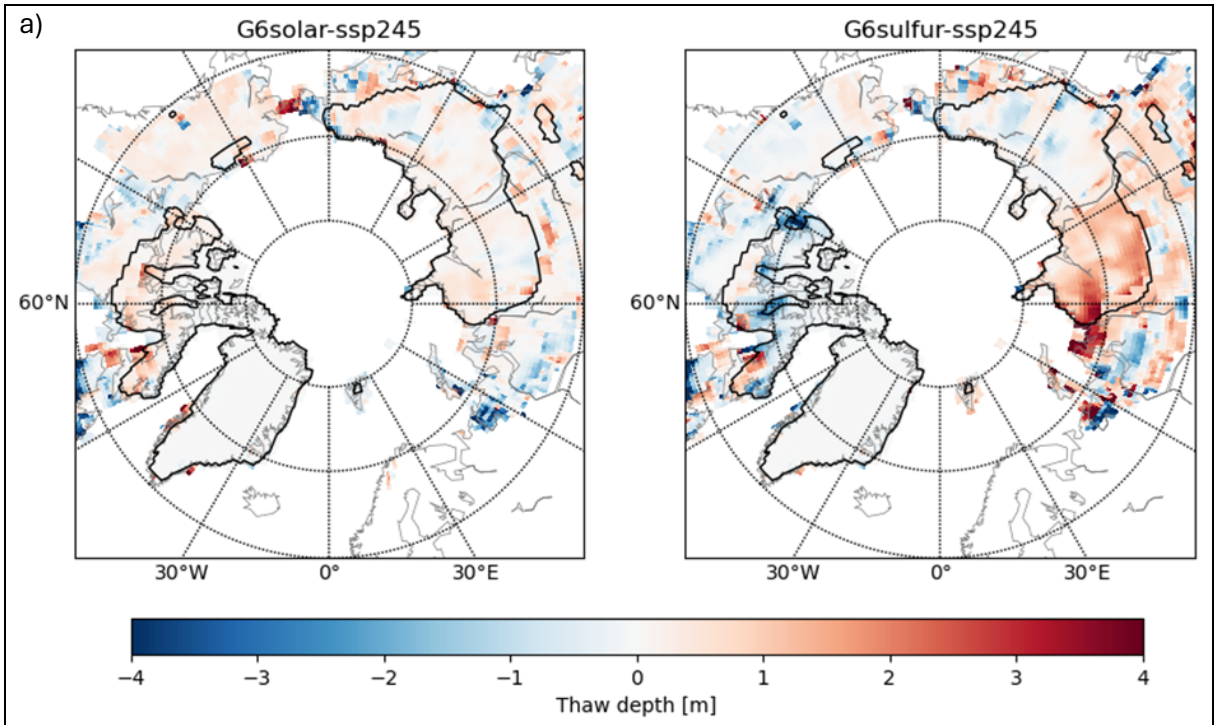

b)

	G6solar-ssp245			G6sulfur-ssp245		
	Thaw Depth (m)	SD (σ)	*P*-value	Thaw Depth (m)	SD (σ)	*P*-value
Northern High Latitudes	+0.10	0.03	<0.05	+0.12	0.03	<0.01
Eastern Hemisphere	+0.15	0.05	<0.05	+0.50	0.05	<0.0001
Western Hemisphere	+0.07	0.03	>0.05	-0.15	0.03	<0.001

Fig. 2: Difference in thaw depth under geoengineering. a) Mean difference in summer (JJA) Thaw Depth (TD) over the period 2080-2099 of G6solar and G6sulfur relative to SSP2-4.5. b) Mean difference in summer (JJA) Thaw Depth per geography, presented with Standard Deviation (SD) and significance level.

3.3 Influence of G6sulfur on summer permafrost thaw depth drivers

To gain insights into the drivers contributing to the observed variations in summer permafrost thaw depth (SPTD) across the Eastern and Western Hemisphere under G6sulfur conditions compared to SSP2-4.5, we conduct both a variance partitioning and a correlation analysis. The

variance partitioning analysis quantifies the predictive ability of each selected driver to explain the difference in SPTD observed between G6sulfur and SSP2-4.5, while the correlation analysis provides information on the strength and direction of the relationships between SPTD and selected drivers. It is important to note that, since we are examining the difference between the geoengineering experiment and the control scenario, the results from the variance partitioning analysis only indicate the difference in explained variance between the two scenarios, not the absolute explained variance. Therefore, in this study, a low explained variance does not necessarily imply that a specific variable is not an important predictor for summer permafrost thaw depth; rather, it means that the explained variance of this variable does not change under geoengineering conditions. The same principle applies to the correlation analysis and further analyses conducted in this study.

The predictors, explaining the difference in SPTD between G6sulfur and SSP2-4.5 in the Eastern Hemisphere, are shown in Figure 3a and 3b. The most important in boreal winter are downwelling longwave radiation (33.6 %), air temperature (31.4 %), and northward wind at 20 hPa (31.3 %). Factors, such as air temperature, mass fraction of cloud liquid water and ice, as well as longwave radiation display a strong positive correlation to SPTD, while zonal and meridional winds have a strong negative relationship (Fig. 3c).

As depicted in Figure 3b, the key summer predictors explaining the difference in SPTD between G6sulfur and SSP2-4.5 are northward wind (37.2 %), eastward wind (30.4 %), mass fraction of cloud ice (30.3 %), and mass fraction of cloud liquid water (23.3 %). During summer, pressure at sea level exhibits a strong positive correlation to SPTD, whereas wind speed, zonal and meridional winds, and cloud composition manifest a strong negative relationship (Fig. 3d).

During the boreal summer, it is important to note that energy fluxes, apart from downwelling longwave radiation (10.4%), are of minimum importance. This observation is particularly intriguing given that G6sulfur is designed to reduce shortwave radiation through stratospheric aerosol injection. Furthermore, summer vegetation, as indicated by the leaf area index, and soil moisture in the upper column play only a minimal role in explaining the difference in SPTD between G6sulfur and SSP2-4.5.

Particularly notable is the complex interplay between cloud water-ice content and thaw depth. We see a positive correlation to SPTD in the winter season and the opposite during summer. Furthermore, the predictors mass fraction of cloud liquid water (Fig. S5c and S5d) and mass fraction of cloud ice (Fig. S7c and S7d) can display positive and negative correlations to SPTD within the same season, depending on the pressure levels of the predictors at which the

correlation is examined. This underscores the complexity and dynamic nature of the involved atmospheric processes.

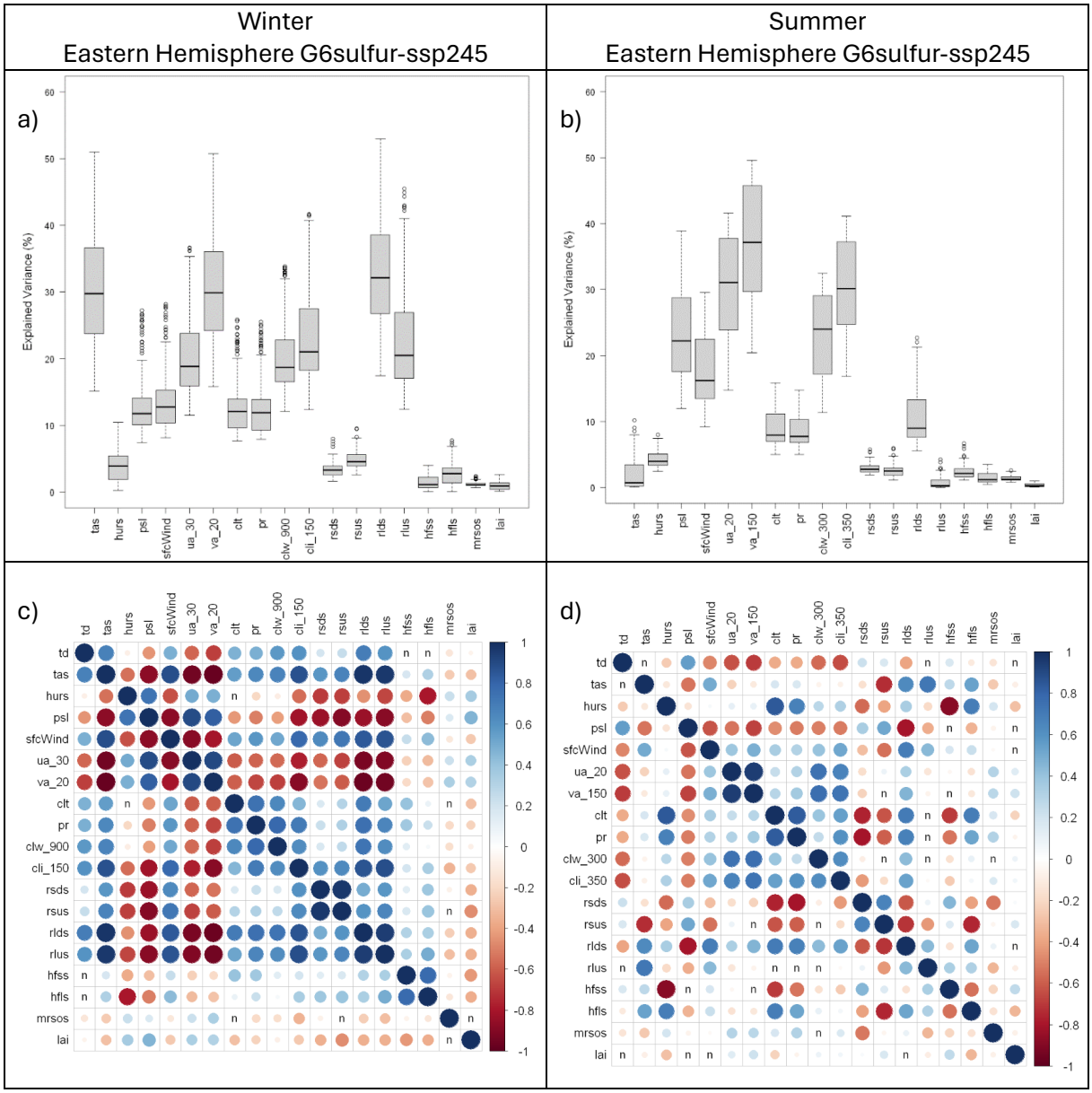

Fig. 3: Influence of G6sulfur on SPTD drivers in Eastern Hemisphere. Top row: explained variance (%) for summer thaw depth (td) per predictor and season over the Eastern Hemisphere for the difference G6sulfur versus SSP2-4.5. Predictors include: tas (air temperature), hurs (relative humidity), psl (air pressure at sea level), sfcWind (surface wind speed), ua (eastward wind at indicated hPa level), va (northward wind at indicated hPa level), clt (cloud cover), pr (precipitation), clw (mass fraction cloud liquid water at indicated hPa level), cli (mass fraction of cloud liquid ice at indicated hPa level), rsds (radiation shortwave downwelling surface), rdus (radiation shortwave upwelling surface), rlds (radiation longwave downwelling surface), rlus (radiation longwave upwelling surface), hfss (sensible heat flux), hfls (latent heat flux), mrsos (moisture in the upper portion of the soil column), lai (leaf area index). a) Drivers from the winter season (DJF) b) Drivers from the summer season (JJA). Bottom row: Correlation matrix of the drivers per season. The direction of the correlation is indicated by the colour, blue for positive correlation, red for negative correlation. The size of the circle represents the strength of the correlation. n in boxes indicates non-significant correlation. c) Winter season (DJF) d) Summer season (JJA).

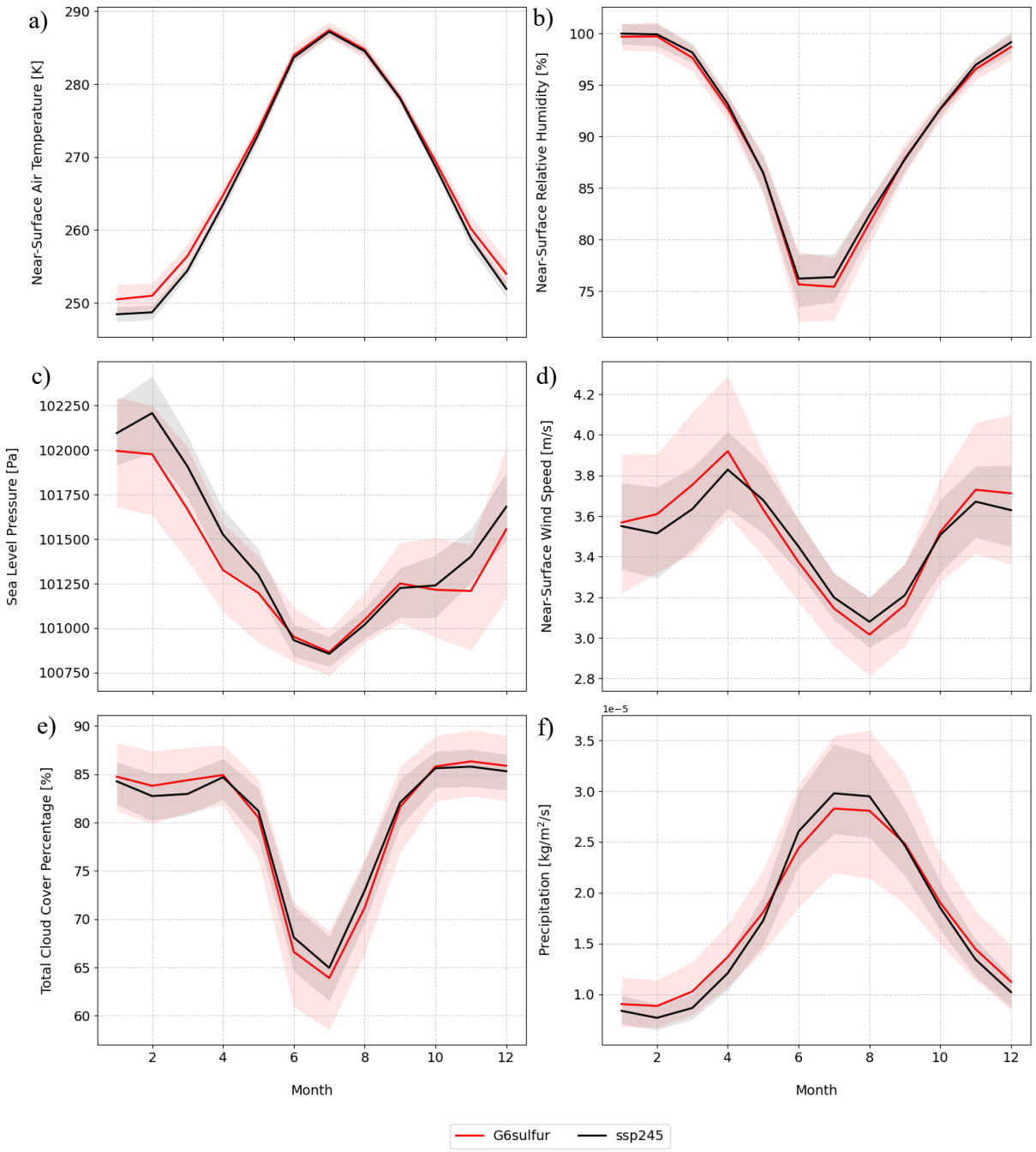

Fig. 4: Meteorological parameters in Eastern Hemisphere monthly mean 2080-2099 a) near-surface air temperature, b) near-surface relative humidity, c) seal level pressure, d) near-surface wind speed, e) total cloud cover percentage, f) precipitation. Shaded areas are max and min values for the respective scenario.

The seasonal patterns over the Eastern Hemisphere in Fig. 4 indicate a shift towards more adverse weather conditions during winter under G6sulfur compared to SSP2-4.5, characterized by higher air temperature, wind speed, cloud cover, and precipitation, along with lower sea level pressure. However, during the summer months, these conditions transition to a more favourable weather pattern with lower humidity, wind speed, reduced cloud cover and precipitation. In

summary, the anomaly forcing from G6sulfur induces a climate shift towards warmer and more adverse winters, contrasting with more favourable weather conditions during summer across the Eastern Hemisphere.

The variance partitioning and correlation analysis for the Western Hemisphere depict a different picture. Unlike in the Eastern Hemisphere, the explanatory power of these predictors (Fig. 5a and 5b) and the correlation (Fig. 5c and 5d) are very limited, with no single predictor exceeding an explained variance of 8.1 % in winter and 5.5 % in summer. At the same time the correlation is weak. These results suggest, that SPTD drivers are very similar in both scenarios, G6sulfur and SSP2-4.5.

Examining the variance partitioning analysis between the G6solar experiment and SSP2-4.5, we note no divergence in the Eastern Hemisphere, implying that the observed results are mainly influenced by aerosol injection, whereas some alterations are seen in the Western Hemisphere (see Fig. S9 and S10 in Supplements).

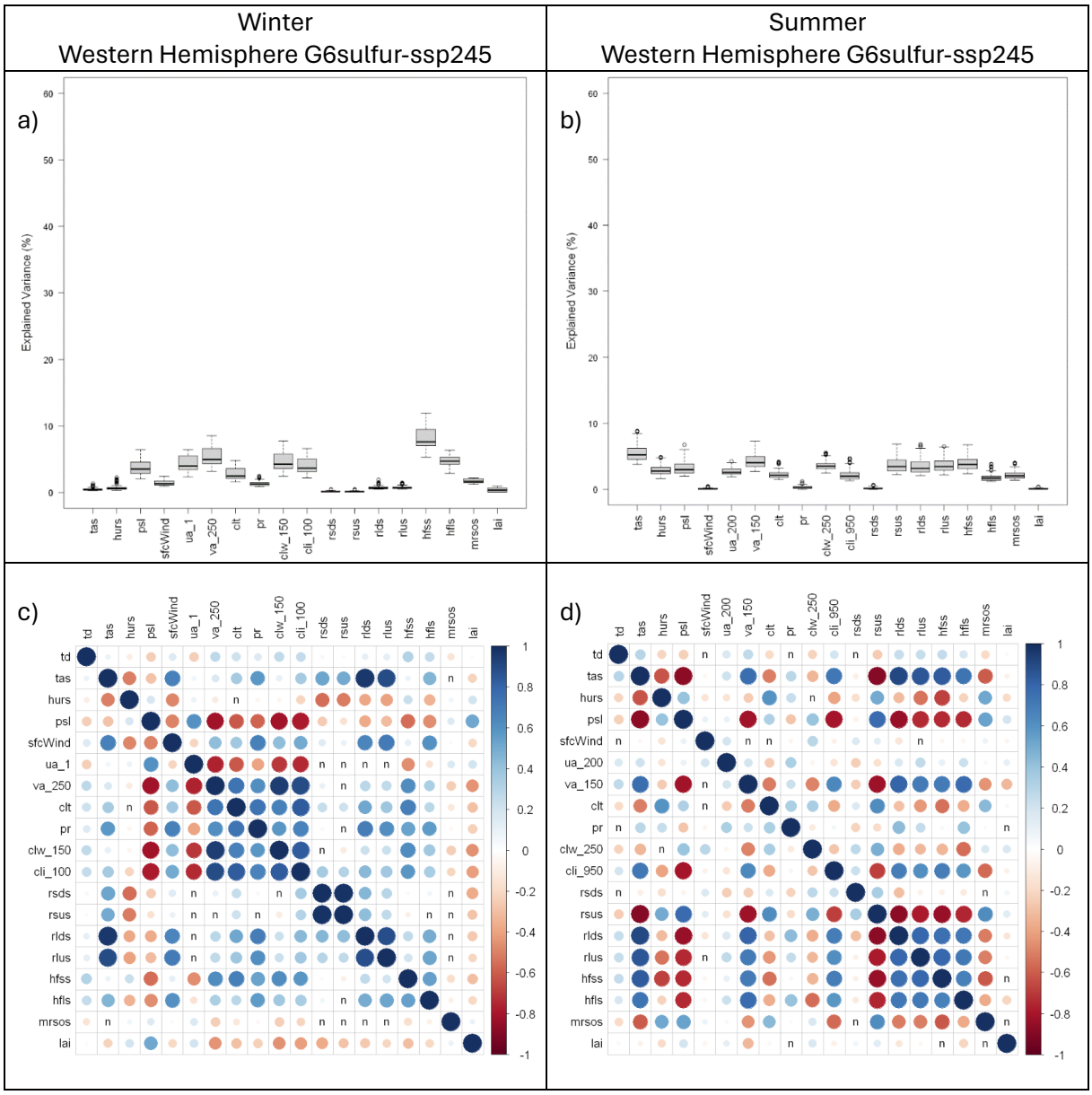

Fig. 5: Influence of G6sulfur on SPTD drivers in Western Hemisphere. Top row: explained variance (%) for summer thaw depth (td) per predictor and season over the Western Hemisphere for the difference G6sulfur versus SSP2-4.5. Predictors include: tas (air temperature), hurs (relative humidity), psl (air pressure at sea level), sfcWind (surface wind speed), ua (eastward wind at indicated hPa level), va (northward wind at indicated hPa level), clt (cloud cover), pr (precipitation), clw (mass fraction cloud liquid water at indicated hPa level), cli (mass fraction of cloud liquid ice at indicated hPa level), rsds (radiation shortwave downwelling surface), rdus (radiation shortwave upwelling surface), rlds (radiation longwave downwelling surface), rlus (radiation longwave upwelling surface), hfss (sensible heat flux), hfls (latent heat flux), mrsos (moisture in the upper portion of the soil column), lai (leaf area index). a) Drivers from the winter season (DJF) b) Drivers from the summer season (JJA). Bottom row: Correlation matrix of the drivers per season. The direction of the correlation is indicated by the colour, blue for positive correlation, red for negative correlation. The size of the circle represents the strength of the correlation. n in boxes indicates non-significant correlation. c) Winter season (DJF) d) Summer season (JJA).

3.4 Influence of G6sulfur on large scale atmospheric patterns

Our variance analysis reveals that the change in winter zonal and meridional winds between G6sulfur and SSP2-4.5 is a key predictor in explaining the variation in summer permafrost thaw depth over the Eastern Hemisphere. Specifically, we observe a strengthening of stratospheric eastward winds under G6sulfur in the latitude band of 50°N to 70°N, with a weakening of eastward flow below 50°N (Fig. 6b). These notable increases are particularly evident over the North Atlantic and the Bering Strait. Additionally, alterations in northward winds are observed, although less pronounced concerning windspeed (Fig. 6c). The difference in wind speed is notably more pronounced in the stratosphere than in the troposphere, as indicated by the data presented in Fig. S11-S14 (see Supplements). This effect is primarily evident under G6sulfur compared to SSP2-4.5 and nearly negligeable under G6solar compared to SSP2-4.5. The spatial distribution of the wind speed anomaly shows increased northward flow in eastern Eurasia and reduced flow in western Eurasia under G6sulfur compared to SSP2-4.5 (Fig. 6c). This geographical pattern bears similarities to the changes in summer permafrost thaw depth observed across the Eastern Hemisphere and presented in section 3.2.

The multi-model ensemble mean of sea level pressure shows a strong perturbation during boreal winter, characterized by a decrease in pressure north of 60° latitude with this negative difference intensifying towards the pole (Fig. 6a). Additionally, zones of high pressure develop around 50°N over the Atlantic Ocean and south of the Bering Strait. Changes over the North American continent and Eurasia are comparatively less pronounced. A similar pressure configuration has been found by Jones et al. (2021) when comparing G6solar to G6sulfur using the CESM2-WACCM6 and UKESM1 models. They associated this pattern with a positive phase of the North Atlantic Oscillation (NAO). Subsequently, in a follow-up study, they found that G6sulfur consistently induces a progressively positive phase of the NAO during wintertime (Jones et al., 2022).

Our analysis reveals a significant strengthening of the pressure gradient during the winter period (DJF) between the Azores and Iceland, with an increase of 6.30 hPa (± 3.35, P-value < 0.0001) and a NAO-Index increase of 1.02 (± 1.10, P-value < 0.0001). While most pronounced in winter, the NAO is one of the few modes of variability that persists throughout the year (Linderholm & Folland, 2017). A positive (negative) summer NAO phase indicates a northward (southward) displacement of tropospheric jets and exerts notable surface climate effects (Dunstone et al., 2023). We observe no significant change in the summer pressure differential when comparing G6sulfur to SSP2-4.5 (Fig. 6e). However, the normalized NAO-Index shows

a significant negative difference of -0.61 (± 0.60, *P*-value < 0.0001), indicating a weakening of the NAO during summer under G6sulfur (Fig. 6f).

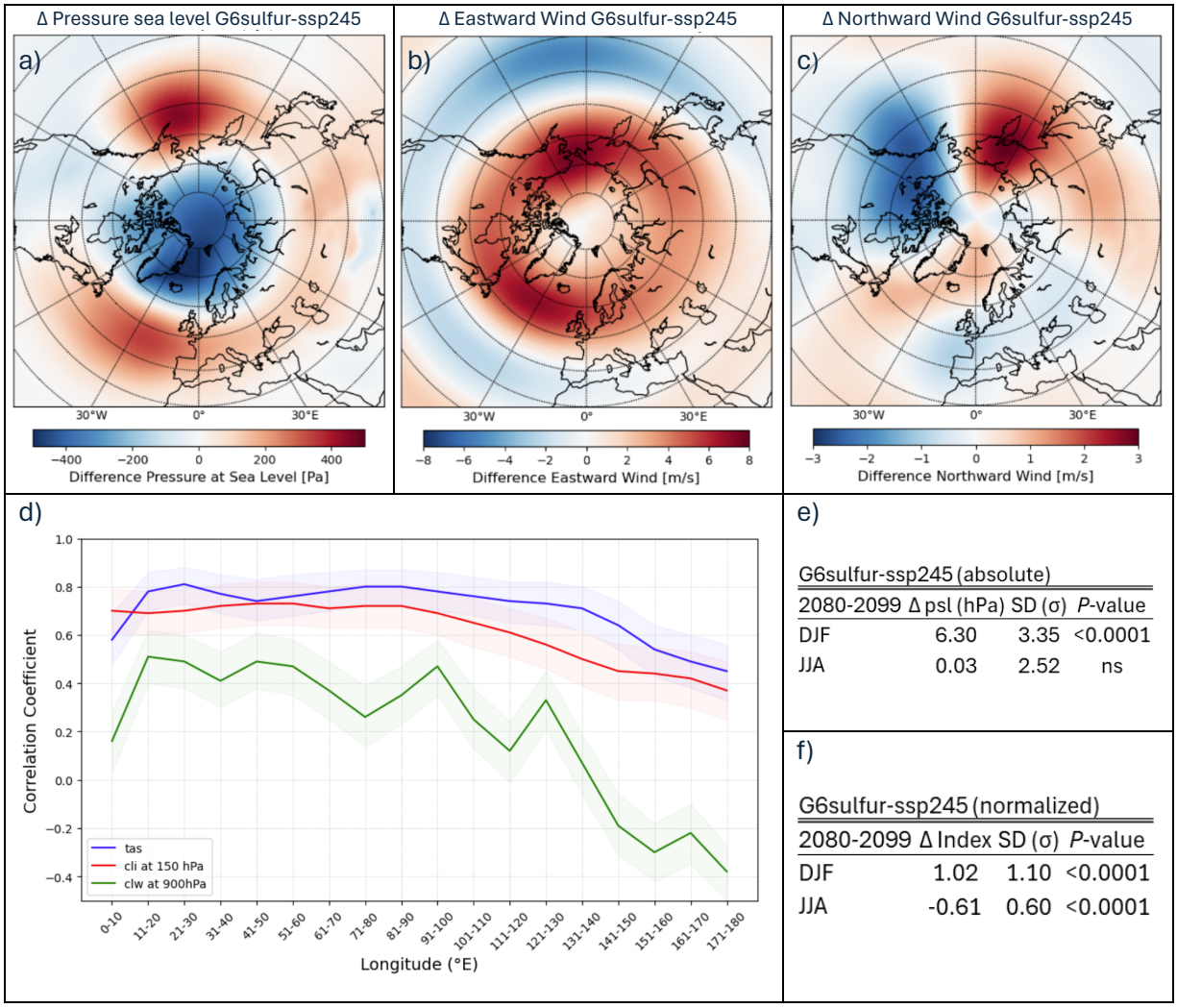

Fig. 6: Influence of G6sulfur on large scale atmospheric patterns. a) Mean winter (DJF) difference in pressure at sea level over the period of 2080-2099 G6sulfur versus SSP2-4.5 b) Mean winter (DJF) difference in eastward wind (average all pressure levels) over the period of 2080-2099 G6sulfur versus SSP2-4.5 c) Mean winter (DJF) difference in northward wind (average all pressure levels) over the period of 2080-2099 G6sulfur versus SSP2-4.5 d) Correlation of North Atlantic Oscillation Index with tas (near surface air temperature), cli (mass fraction of cloud ice at 150 hPa) and clw (mass fraction of cloud liquid water at 900 hPa) per longitude segment with a latitude from 65°N-75°N, shaded area 95% confidence level. e) Absolute difference in pressure at sea level between the Azores and Island during winter (DJF) and summer (JJA) over the period 2080-2099, ns=non-significant f) Normalized difference in pressure at sea level between the Azores and Island during winter (DJF) and summer (JJA) over the period 2080-2099.

In addition to the changes in pressure difference and normalized index induced by G6sulfur during winter and summer, the NAO correlates with important predictors that explain the variance of summer permafrost thaw depth over the Eastern Hemisphere (Figure 6d). This

correlation, based on a 3-month rolling normalized average, is particularly strong for air temperature and the mass fraction of cloud ice, and to a lesser extent for cloud liquid water. These interrelations weaken with increasing eastward longitude. Our results suggest, that G6sulfur is creating a large-scale atmospheric pattern change with a positive NAO-Index in winter and negative in summer influencing the SPTD by altering the eastward air mass transport from the Atlantic Ocean over the Eurasian continent, modifying its effect with increasing longitude as the air travels over land and changes its physical properties.

4 Discussion

Our study shows that permafrost area is declining more rapidly ($-1.12 \pm 0.57 \times 10^6$ km^2, *P*-value < 0.0001) and the summer permafrost thaw depth is increasing ($+0.12 \pm 0.03$ m, *P*-value < 0.01) under G6sulfur compared to the SSP2-4.5 control scenario. A comparable finding, albeit with a different pathway as control, was published by Müller et al. (2024), who reported that Arctic land with temperatures below freezing is projected to decline by 7.8% by the end of the century when comparing SAI to RCP4.5.

Furthermore, our study revealed a notable spatial divergence: in the Eastern Hemisphere, there is a pronounced retreat of permafrost area along with deeper summer permafrost thaw depths, whereas the Western Hemisphere exhibits a slight increase in permafrost area accompanied by slightly shallower summer permafrost thaw depths. The observed increase in permafrost decline in Western Siberia due to stratospheric aerosol injection under G6sulfur, as highlighted in our study, is particularly significant. Grysko et al. (2024) noted that this region already experiences the strongest positive spring temperature trend in the Arctic, exceeding 1°C per decade, and the strength has risen for heat extremes and declined for cold extremes. This implies a pre-existing warming pattern attributed to rising CO_2 emissions, which exacerbates with the addition of G6sulfur. There may be an underlying mechanism driven by the CO_2 content in the atmosphere connecting these observations, meriting additional investigation.

The regional difference in permafrost extent and summer permafrost thaw depth is accompanied by an evident shift in the relative significance of various permafrost drivers in the Eastern Arctic. Whereas in the Western Arctic, the importance of different summer permafrost thaw drivers remains relatively similar to SSP2-4.5. In the Eastern Hemisphere, the differences in predictive ability of the different drivers for summer permafrost thaw depth between G6sulfur and SSP2-4.5, show that the largest variations are observed in atmospheric variables such as zonal and meridional winds, cloud water and ice content, and the North Atlantic Oscillation (NAO) in both winter and summer, thereby influencing temperature variations as well as the reflection and absorption of longwave radiation. This implies that stratospheric aerosol injections under the G6sulfur scenario cause substantial alterations in atmospheric circulation patterns at high latitudes during both boreal winter and summer. Previous studies by Banerjee et al. (2021) and Chen et al. (2023) have documented a residual winter warming phenomenon at high latitudes under SAI, resulting in increased temperatures during the boreal winter. Furthermore, research by Jones et al. (2021) showed a positive anomaly in the NAO during the winter season in the Northern Hemisphere under the G6sulfur scenario, indicating intensified

zonal flow and enhanced North Atlantic storm track activity. These changes have implications for the Eastern Hemisphere, leading to high latitude warming over Europe and Asia. Similar effects have been observed with stratospheric volcanic aerosols resulting from volcanic eruptions in the tropics (Shindell et al., 2004), indicating that the changes produced by the models under G6sulfur are likely to be solid.

The results of our study provide further support for the observed phenomena, revealing a pronounced sea level pressure gradient from the Azores to Iceland during boreal winter under G6sulfur. This suggests a shift towards a more positive North Atlantic Oscillation and an important intensification of the eastward wind pattern. Additionally, we observe a shift to a more negative North Atlantic Oscillation under G6sulfur during summer. These changes in strength and direction of the NAO show a strong correlation with air temperature, as well as the mass fraction of cloud ice, and to a lesser extent, the mass fraction of cloud liquid water over the Eastern Arctic. The correlations weaken with increasing longitude across the Eurasian continent.

The interactions between cloud properties as well as zonal and meridional winds on different pressure levels present a complex interplay that influences permafrost thaw dynamics. We have identified a positive correlation between cloud cover, the mass fraction of cloud liquid water and ice during wintertime and the summer thaw depth of permafrost. This suggests that clouds enhance summer permafrost thaw depths, likely due to the reflection of upwelling longwave radiation by ice crystals and water droplets, creating a longwave trapping effect during wintertime. This observation of increased downwelling longwave radiation is consistent with findings from Boisvert & Stroeve (2015) and Shupe & Intrieri (2004). Conversely, during summertime, a negative correlation is observed between cloud cover as well as the mass fraction of cloud water and ice and summer permafrost thaw depth across various pressure levels, indicating a protective effect of clouds during this season. The varying strengths of this negative correlation highlight the complex nature of cloud-permafrost interactions. This protective effect during summer may be attributed to the reflection of sunlight by cloud layers back into space. These findings align with Alkama et al. (2020) who reported a 47% overall damping effect of clouds over Arctic sea ice decline.

It is plausible to assume that the implementation of G6sulfur induces a significant alteration in large-scale atmospheric patterns, particularly characterized by an amplification of the North Atlantic Oscillation during boreal winter. This phenomenon results in a heightened eastward flow of moist and warmer air masses originating from the Atlantic Ocean, thereby contributing

to elevated temperatures and increased cloud cover over the Eurasian region. The intensified cloud cover, potentially containing higher concentrations of liquid water or ice particles, acts as an effective barrier to the escape of upwelling longwave radiation into space. This, combined with higher temperatures, contributes to an increased retention of heat within the atmosphere. As a result, a considerable portion of the longwave radiation is reflected back towards the earth's surface, effectively creating a mechanism akin to a longwave trapping effect. These combined atmospheric changes lead to elevated temperatures and enhanced energy fluxes at the surface, ultimately contributing to an increased summer permafrost thaw depth over the high latitude Eastern Hemisphere. As the air mass moves further over Eurasia, the effectiveness of this mechanism may diminish. The air mass tends to dry up and cool as it traverses over land, leading to a reduction in moisture content and thermal properties. Consequently, the intensity of the longwave trapping effect diminishes, and the associated increase in summer permafrost thaw depth may be less pronounced, particularly over inland regions or after mountain ridges where the air mass has undergone significant drying and cooling processes.

Whereas boreal winter is marked by a positive NAO, G6sulfur induces a more negative NAO during boreal summer. It can be hypothesized that there is a decrease in zonal flow and fewer humid air masses arriving from the Atlantic Ocean. This could lead to a more favourable weather pattern characterized by lower humidity, reduced wind speed, diminished cloud cover, and decreased precipitation. However, this scenario may also pose potential drawbacks, as the soil becomes less protected by clouds, resulting in less reflection of incoming shortwave radiation by clouds back into space and therefore negatively impacting the summer permafrost thaw depth.

Summer shortwave energy fluxes seem to have only a very limited predictive power in explaining the difference in summer permafrost thaw depth between G6sulfur and SSP2-4.5. While there is a reduction in net shortwave radiation over the Eastern Arctic during boreal summer under G6sulfur, this change does not significantly contribute to the difference in thaw depth between G6sulfur and SSP2-4.5. This observation may seem counterintuitive, given that SAI aims to reduce incoming shortwave radiation from the sun. This raises the question of whether a different injection strategy closer to the polar regions, with a higher concentration of SO_4 and consequently a higher aerosol optical depth at high latitudes, would yield different outcomes.

It's crucial to acknowledge the inherent variability in model response of the six ESMs used in this study. Visioni et al. (2021) found that, across the final two decades of the century, significant

disparities emerge among models in terms of required sulphate injection amounts (29 ± 9 Tg SO_2/yr between 2081 and 2100), the latitudinal distribution of the aerosol cloud, and resultant stratospheric temperature changes. Even within the simpler G6solar experiment, there is variation in the level of solar dimming necessary to achieve the same global temperature target. This highlights the necessity of further improving and refining the model techniques, particularly crucial for accurately representing complex phenomena like permafrost freeze-thaw dynamics.

5 Conclusion

In conclusion, the G6sulfur by experimental design brings the radiative forcing from SSP5-8.5 to SSP2-4.5 levels by introducing stratospheric aerosols along a single longitude band from 10°S to 10°N. While achieving the targeted global forcing of -4 W/m^2, G6sulfur appears to be a practicable option for preserving permafrost in the Western Arctic. However, it is inducing a large-scale atmospheric pattern change which tends to a faster decrease of the total high latitude permafrost area, together with an increase of summer permafrost thaw depth, compared to the SSP2-4.5 reference, which has specifically a detrimental effect over the Eastern Arctic. Our study contributes to a better understanding of the mechanisms underlying these changes, revealing the complex interactions between geoengineering interventions and environmental processes.

Although the coordinated GeoMIP6 experiments outlined in this study provide valuable insights, it is essential to acknowledge that they represent only one approach to SAI deployment and may not be the most optimal for various reasons (Visioni et al., 2021). The impacts of stratospheric aerosol injection largely depend on the spatial and temporal patterns of aerosol optical depth. This opens a variety of strategic injection choices regarding season, location, quantity, and altitude. Visioni et al. (2019) suggest that injecting aerosols throughout the year may not be optimal, as seasonal distribution could significantly impact climatic effects. Research by Kravitz et al. (2019) and MacMartin et al. (2017) demonstrate that alternative approaches, like dispersing aerosols at different locations beyond low latitudes could offer better control over the spatial distribution of aerosol optical depth. This potentially leads to enhanced results by more efficiently regulating global mean temperatures, inter-hemispheric gradients, and temperature variations from the equator to the poles. Furthermore, W. R. Lee et al. (2023) investigated high-latitude injection strategies at 60°N concentrated over the months of March, April, and May. They found that such strategies have a more pronounced impact on cooling at the pole compared to a globally focused SAI strategy that injects similar quantities of SO_2 at lower latitudes, thereby mitigating, but not eliminating, the large-scale climate pattern changes induced by SAI at lower latitudes. Studying the impact of different injection strategies on the drivers influencing summer permafrost thaw depth emerges as an important area for future research. Through these investigations, we gain valuable insights into the factors affecting permafrost dynamics and improve our understanding of the effectiveness and potential consequences of various stratospheric aerosol injection strategies.

6 References

ACGR. (1988). Glossary of permafrost and related ground-ice terms. In *National Research Council of Canada, Associate Committee on Geotechnical Research, Technical Memorandum 142*. https://doi.org/10.4224/20386561

Alkama, R., Taylor, P. C., Garcia-San Martin, L., Douville, H., Duveiller, G., Forzieri, G., Swingedouw, D., & Cescatti, A. (2020). Clouds damp the radiative impacts of polar sea ice loss. *Cryosphere*, *14*(8), 2673–2686. https://doi.org/10.5194/tc-14-2673-2020

Banerjee, A., Butler, A. H., Polvani, L. M., Robock, A., Simpson, I. R., & Sun, L. (2021). Robust winter warming over Eurasia under stratospheric sulfate geoengineering - The role of stratospheric dynamics. *Atmospheric Chemistry and Physics*, *21*(9), 6985–6997. https://doi.org/10.5194/acp-21-6985-2021

Biskaborn, B. K., Smith, S. L., Noetzli, J., Matthes, H., Vieira, G., Streletskiy, D. A., Schoeneich, P., Romanovsky, V. E., Lewkowicz, A. G., Abramov, A., Allard, M., Boike, J., Cable, W. L., Christiansen, H. H., Delaloye, R., Diekmann, B., Drozdov, D., Etzelmüller, B., Grosse, G., … Lantuit, H. (2019). Permafrost is warming at a global scale. *Nature Communications*, *10*(1). https://doi.org/10.1038/s41467-018-08240-4

Boisvert, L. N., & Stroeve, J. C. (2015). The Arctic is becoming warmer and wetter as revealed by the Atmospheric Infrared Sounder. *Geophysical Research Letters*, *42*(11), 4439–4446. https://doi.org/10.1002/2015GL063775

Burke, E. J., Zhang, Y., & Krinner, G. (2020). Evaluating permafrost physics in the Coupled Model Intercomparison Project 6 (CMIP6) models and their sensitivity to climate change. *Cryosphere*, *14*(9), 3155–3174. https://doi.org/10.5194/tc-14-3155-2020

Chadburn, S. E., Burke, E. J., Cox, P. M., Friedlingstein, P., Hugelius, G., & Westermann, S. (2017). An observation-based constraint on permafrost loss as a function of global warming. *Nature Climate Change*, *7*(5), 340–344. https://doi.org/10.1038/nclimate3262

Chadburn, S. E., Burke, E. J., Essery, R. L. H., Boike, J., Langer, M., Heikenfeld, M., Cox, P. M., & Friedlingstein, P. (2015). Impact of model developments on present and future simulations of permafrost in a global land-surface model. *Cryosphere*, *9*(4), 1505–1521. https://doi.org/10.5194/tc-9-1505-2015

Chen, Y., Ji, D., Zhang, Q., Moore, J. C., Boucher, O., Jones, A., Lurton, T., Mills, M. J., Niemeier, U., Séférian, R., & Tilmes, S. (2023a). Northern-high-latitude permafrost and terrestrial carbon response to two solar geoengineering scenarios. *Earth System Dynamics*, *14*(1), 55–79. https://doi.org/10.5194/esd-14-55-2023

Chen, Y., Ji, D., Zhang, Q., Moore, J. C., Boucher, O., Jones, A., Lurton, T., Mills, M. J., Niemeier, U., Séférian, R., & Tilmes, S. (2023b). Northern-high-latitude permafrost and terrestrial carbon response to two solar geoengineering scenarios. *Earth System Dynamics*, *14*(1), 55–79. https://doi.org/10.5194/esd-14-55-2023

Chen, Y., Liu, A., & Moore, J. C. (2020). Mitigation of Arctic permafrost carbon loss through stratospheric aerosol geoengineering. *Nature Communications*, *11*(1). https://doi.org/10.1038/s41467-020-16357-8

Dunstone, N., Smith, D. M., Hardiman, S. C., Hermanson, L., Ineson, S., Kay, G., Li, C., Lockwood, J. F., Scaife, A. A., Thornton, H., Ting, M., & Wang, L. (2023). Skilful predictions of the Summer North Atlantic Oscillation. *Communications Earth and Environment*, *4*(1). https://doi.org/10.1038/s43247-023-01063-2

Eugster, W., Rouse, W. R., Pielke, R. A., Mcfadden, J. P., Baldocchi, D. D., Kittel, T. G. F., Chapin, F. S., Liston, G. E., Vidale, P. L., Vaganov, E., & Chambers, S. (2000). Land-atmosphere energy exchange in Arctic tundra and boreal forest: Available data and feedbacks to climate. *Global Change Biology*, *6*(SUPPLEMENT 1), 84–115. https://doi.org/10.1046/j.1365-2486.2000.06015.x

Gallet, J. C., Domine, F., Arnaud, L., Picard, G., & Savarino, J. (2011). Vertical profile of the specific surface area and density of the snow at Dome C and on a transect to Dumont D'Urville, Antarctica - Albedo calculations and comparison to remote sensing products. *Cryosphere*, *5*(3), 631–649. https://doi.org/10.5194/tc-5-631-2011

Garnello, A., Marchenko, S., Nicolsky, D., Romanovsky, V., Ledman, J., Celis, G., Schädel, C., Luo, Y., & Schuur, E. A. G. (2021). Projecting Permafrost Thaw of Sub-Arctic Tundra With a Thermodynamic Model Calibrated to Site Measurements. *Journal of Geophysical Research: Biogeosciences*, *126*(6). https://doi.org/10.1029/2020JG006218

Gruber, S. (2012). Derivation and analysis of a high-resolution estimate of global permafrost zonation. *Cryosphere*, *6*(1), 221–233. https://doi.org/10.5194/tc-6-221-2012

Grysko, R., Kim, J. S., & Schaepman-Strub, G. (2024). Arctic springtime temperature and energy flux interannual variability is driven by 1- to 2-week frequency atmospheric events. *Weather and Climate Extremes*, *43*. https://doi.org/10.1016/j.wace.2024.100650

Hugelius, G., Strauss, J., Zubrzycki, S., Harden, J. W., Schuur, E. A. G., Ping, C. L., Schirrmeister, L., Grosse, G., Michaelson, G. J., Koven, C. D., O'Donnell, J. A., Elberling, B., Mishra, U., Camill, P., Yu, Z., Palmtag, J., & Kuhry, P. (2014). Estimated stocks of circumpolar permafrost carbon with quantified uncertainty ranges and identified data gaps. *Biogeosciences*, *11*(23), 6573–6593. https://doi.org/10.5194/bg-11-6573-2014

Jiang, J., Cao, L., MacMartin, D. G., Simpson, I. R., Kravitz, B., Cheng, W., Visioni, D., Tilmes, S., Richter, J. H., & Mills, M. J. (2019). Stratospheric Sulfate Aerosol Geoengineering Could Alter the High-Latitude Seasonal Cycle. *Geophysical Research Letters*, *46*(23), 14153–14163. https://doi.org/10.1029/2019GL085758

Jones, A., Haywood, J. M., Jones, A. C., Tilmes, S., Kravitz, B., & Robock, A. (2021). North Atlantic Oscillation response in GeoMIP experiments G6solar and G6sulfur: Why detailed modelling is needed for understanding regional implications of solar radiation management. *Atmospheric Chemistry and Physics*, *21*(2), 1287–1304. https://doi.org/10.5194/acp-21-1287-2021

Jones, A., Haywood, J. M., Scaife, A. A., Boucher, O., Henry, M., Kravitz, B., Lurton, T., Nabat, P., Niemeier, U., Séférian, R., Tilmes, S., & Visioni, D. (2022). The impact of stratospheric aerosol intervention on the North Atlantic and Quasi-Biennial Oscillations in the Geoengineering Model Intercomparison Project (GeoMIP) G6sulfur experiment. *Atmospheric Chemistry and Physics*, *22*(5), 2999–3016. https://doi.org/10.5194/acp-22-2999-2022

Kravitz, B., MacMartin, D. G., Tilmes, S., Richter, J. H., Mills, M. J., Cheng, W., Dagon, K., Glanville, A. S., Lamarque, J. F., Simpson, I. R., Tribbia, J., & Vitt, F. (2019). Comparing Surface and Stratospheric Impacts of Geoengineering With Different SO2 Injection Strategies. *Journal of Geophysical Research: Atmospheres*, *124*(14), 7900–7918. https://doi.org/10.1029/2019JD030329

Kravitz, B., Robock, A., Tilmes, S., Boucher, O., English, J. M., Irvine, P. J., Jones, A., Lawrence, M. G., MacCracken, M., Muri, H., Moore, J. C., Niemeier, U., Phipps, S. J., Sillmann, J., Storelvmo, T., Wang, H., & Watanabe, S. (2015). The Geoengineering Model Intercomparison Project Phase 6 (GeoMIP6): Simulation design and preliminary results. *Geoscientific Model Development*, *8*(10), 3379–3392. https://doi.org/10.5194/gmd-8-3379-2015

Lee, H., Ekici, A., Tjiputra, J., Muri, H., Chadburn, S. E., Lawrence, D. M., & Schwinger, J. (2019). The Response of Permafrost and High-Latitude Ecosystems Under Large-Scale Stratospheric Aerosol Injection and Its Termination. *Earth's Future*, *7*(6), 605–614. https://doi.org/10.1029/2018EF001146

Lee, W. R., MacMartin, D. G., Visioni, D., Kravitz, B., Chen, Y., Moore, J. C., Leguy, G., Lawrence, D. M., & Bailey, D. A. (2023). High-Latitude Stratospheric Aerosol Injection to Preserve the Arctic. *Earth's Future*, *11*(1). https://doi.org/10.1029/2022EF003052

Linderholm, H. W., & Folland, C. K. (2017). Summer North Atlantic Oscillation (SNAO) variability on decadal to palaeoclimate time scales. *Past Global Changes Magazine*, *25*(1), 57–60. https://doi.org/10.22498/pages.25.1.57

Liu, A., Moore, J. C., & Chen, Y. (2023). PInc-PanTher estimates of Arctic permafrost soil carbon under the GeoMIP G6solar and G6sulfur experiments. *Earth System Dynamics*, *14*(1), 39–53. https://doi.org/10.5194/esd-14-39-2023

Macmartin, D. G., Kravitz, B., Tilmes, S., Richter, J. H., Mills, M. J., Lamarque, J. F., Tribbia, J. J., & Vitt, F. (2017). The climate response to stratospheric aerosol geoengineering can be tailored using multiple injection locations. *Journal of Geophysical Research: Atmospheres*, *122*(23), 12,574-12,590. https://doi.org/10.1002/2017JD026868

Make Sunsets. (n.d.). Retrieved April 18, 2023, from https://makesunsets.com/

McGuire, A. D., Lawrence, D. M., Koven, C., Clein, J. S., Burke, E., Chen, G., Jafarov, E., Macdougall, A. H., Marchenko, S., Nicolsky, D., Peng, S., Rinke, A., Ciais, P., Gouttevin, I., Hayes, D. J., Ji, D., Krinner, G., Moore, J. C., Romanovsky, V., … Zhuang, Q. (2018). *Dependence of the evolution of carbon dynamics in the northern permafrost region on the trajectory of climate change*. https://doi.org/10.5067/ZRL5WJKN01XM

McKay, D. I. A., Staal, A., Abrams, J. F., Winkelmann, R., Sakschewski, B., Loriani, S., Fetzer, I., Cornell, S. E., Rockström, J., & Lenton, T. M. (2022). Exceeding 1.5°C global warming could trigger multiple climate tipping points. *Science*, *377*(6611). https://doi.org/10.1126/science.abn7950

Müller, R. C., Kim, J. S., Lee, H., Muri, H., Tjiputra, J., Yoon, J. H., & Schaepman-Strub, G. (2024). Radiative forcing geoengineering causes higher risk of wildfires and permafrost thawing over the Arctic regions. *Communications Earth and Environment*, *5*(1). https://doi.org/10.1038/s43247-024-01329-3

Niemeier, U., & Schmidt, H. (2017). Changing transport processes in the stratosphere by radiative heating of sulfate aerosols. *Atmospheric Chemistry and Physics*, *17*(24), 14871–14886. https://doi.org/10.5194/acp-17-14871-2017

Obu, J. (2021). How Much of the Earth's Surface is Underlain by Permafrost? In *Journal of Geophysical Research: Earth Surface* (Vol. 126, Issue 5). Blackwell Publishing Ltd. https://doi.org/10.1029/2021JF006123

Oehri, J., Schaepman-Strub, G., Kim, J. S., Grysko, R., Kropp, H., Grünberg, I., Zemlianskii, V., Sonnentag, O., Euskirchen, E. S., Reji Chacko, M., Muscari, G., Blanken, P. D., Dean, J. F., di Sarra, A., Harding, R. J., Sobota, I., Kutzbach, L., Plekhanova, E., Riihelä, A., … Chambers, S. D. (2022). Vegetation type is an important predictor of the arctic summer land surface energy budget. *Nature Communications*, *13*(1). https://doi.org/10.1038/s41467-022-34049-3

Ohta, T., Maximov, T. C., Dolman, A. J., Nakai, T., van der Molen, M. K., Kononov, A. V., Maximov, A. P., Hiyama, T., Iijima, Y., Moors, E. J., Tanaka, H., Toba, T., & Yabuki, H. (2008). Interannual variation of water balance and summer evapotranspiration in an eastern Siberian larch forest over a 7-year period (1998-2006). *Agricultural and Forest Meteorology*, *148*(12), 1941–1953. https://doi.org/10.1016/j.agrformet.2008.04.012

Osterkamp, T. E. (2007). Characteristics of the recent warming permafrost in Alaska. *Journal of Geophysical Research: Earth Surface*, *112*(2). https://doi.org/10.1029/2006JF000578

Rantanen, M., Karpechko, A. Y., Lipponen, A., Nordling, K., Hyvärinen, O., Ruosteenoja, K., Vihma, T., & Laaksonen, A. (2022). The Arctic has warmed nearly four times faster than the globe since 1979. *Communications Earth and Environment*, *3*(1). https://doi.org/10.1038/s43247-022-00498-3

Schneider Von Deimling, T., Meinshausen, M., Levermann, A., Huber, V., Frieler, K., Lawrence, D. M., & Brovkin, V. (2012). Estimating the near-surface permafrost-carbon feedback on global warming. *Biogeosciences*, *9*(2), 649–665. https://doi.org/10.5194/bg-9-649-2012

SCoPEX. (n.d.). Retrieved April 26, 2023, from https://www.keutschgroup.com/scopex

Shindell, D. T., Schmidt, G. A., Mann, M. E., & Faluvegi, G. (2004). Dynamic winter climate response to large tropical volcanic eruptions since 1600. *Journal of Geophysical Research: Atmospheres*, *109*(5). https://doi.org/10.1029/2003jd004151

Shupe, M. D., & Intrieri, J. M. (2004). Cloud Radiative Forcing of the Arctic Surface: The Influence of Cloud Properties, Surface Albedo, and Solar Zenith Angle. *Journal of Climate*, *17*, 616–628.

Stieglitz, M., Déry, S. J., Romanovsky, V. E., & Osterkamp, T. E. (2003). The role of snow cover in the warming of arctic permafrost. *Geophysical Research Letters*, *30*(13). https://doi.org/10.1029/2003GL017337

Strauss, J., Schirrmeister, L., Grosse, G., Fortier, D., Hugelius, G., Knoblauch, C., Romanovsky, V., Schädel, C., Schneider von Deimling, T., Schuur, E. A. G., Shmelev, D., Ulrich, M., & Veremeeva, A. (2017). Deep Yedoma permafrost: A synthesis of depositional characteristics and carbon vulnerability. In *Earth-Science Reviews* (Vol. 172, pp. 75–86). Elsevier B.V. https://doi.org/10.1016/j.earscirev.2017.07.007

Sturm, M. (2005). Changing snow and shrub conditions affect albedo with global implications. *Journal of Geophysical Research*, *110*(G1). https://doi.org/10.1029/2005jg000013

The Geoengineering Model Intercomparison Project (GeoMIP). (n.d.). Retrieved May 24, 2023, from http://climate.envsci.rutgers.edu/geomip/about.html

Tilmes, S., Mills, M. J., Niemeier, U., Schmidt, H., Robock, A., Kravitz, B., Lamarque, J. F., Pitari, G., & English, J. M. (2015). A new geoengineering model intercomparison project (GeoMIP) experiment designed for climate and chemistry models. *Geoscientific Model Development*, *8*(1), 43–49. https://doi.org/10.5194/gmd-8-43-2015

Van Huissteden, J. (2020). Thawing permafrost: Permafrost carbon in a warming arctic. In *Thawing Permafrost: Permafrost Carbon in a Warming Arctic*. Springer International Publishing. https://doi.org/10.1007/978-3-030-31379-1

Visioni, D., Kravitz, B., Robock, A., Tilmes, S., Haywood, J., Boucher, O., Lawrence, M., Irvine, P., Niemeier, U., Xia, L., Chiodo, G., Lennard, C., Watanabe, S., Moore, J. C., & Muri, H. (2023). Opinion: The scientific and community-building roles of the Geoengineering Model Intercomparison Project (GeoMIP) – past, present, and future. *Atmospheric Chemistry and Physics*, *23*(9), 5149–5176. https://doi.org/10.5194/acp-23-5149-2023

Visioni, D., Macmartin, D. G., Kravitz, B., Boucher, O., Jones, A., Lurton, T., Martine, M., Mills, M. J., Nabat, P., Niemeier, U., Séférian, R., & Tilmes, S. (2021). Identifying the sources of uncertainty in climate model simulations of solar radiation modification with the G6sulfur and G6solar Geoengineering Model Intercomparison Project (GeoMIP) simulations. *Atmospheric Chemistry and Physics*, *21*(13), 10039–10063. https://doi.org/10.5194/acp-21-10039-2021

Visioni, D., MacMartin, D. G., Kravitz, B., Tilmes, S., Mills, M. J., Richter, J. H., & Boudreau, M. P. (2019). Seasonal Injection Strategies for Stratospheric Aerosol Geoengineering. *Geophysical Research Letters*, *46*(13), 7790–7799. https://doi.org/10.1029/2019GL083680

7 Acknowledgment

I would like to take this opportunity to express my gratitude to everyone who supported me throughout the process of completing this master thesis. First, I want to thank my supervisor, Prof. Dr. Gabriela Schaepman-Strub, for her guidance and opportunity to delve into this topic, including the opportunity to attend the Arctic Science Summit Week in both 2023 and 2024. Further, I am also very grateful to Rhonda Müller and Raleigh Grysko for their continuous help and support throughout this last year, and to Jacqueline Oehri for providing me her codes and support for the variance partitioning analysis. Additionally, I appreciate Prof. Dr. Jin-Soo Kim for his advise and support. Lastly, I want to thank Guido Businger and Valérie Schaerer-Businger for dedicating their time to proofread my thesis.

8 Supplements

8.1 Eastward Wind in Eastern Hemisphere

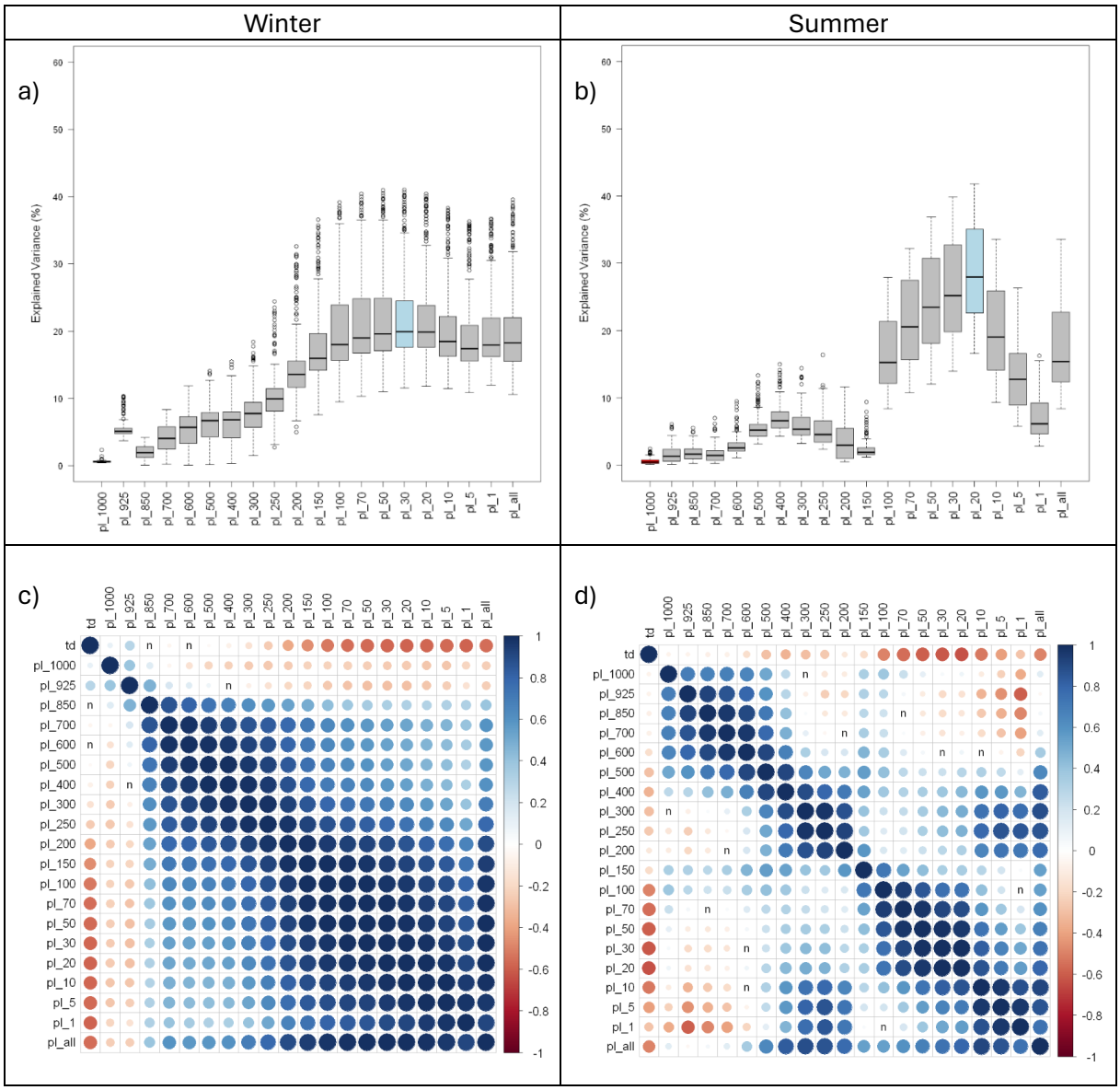

Fig. S1: Top row: explained variance in % for summer thaw depth (td) by eastward wind per hPa level over the Eastern Hemisphere. Blue and red are highest, respectively, lowest variance. a) Winter eastward wind (DJF), b) Summer eastward wind (JJA). Bottom row: Correlation of eastward wind on different pressure levels (in hPa) with summer thaw depth over eastern Hemisphere. Direction of the correlation: blue is positive, red is negative. Strength of correlation is represented by the size of the circle. n in boxes stands for non-significant c) Winter (DJF) d) Summer (JJA).

8.2 Eastward Wind in Western Hemisphere

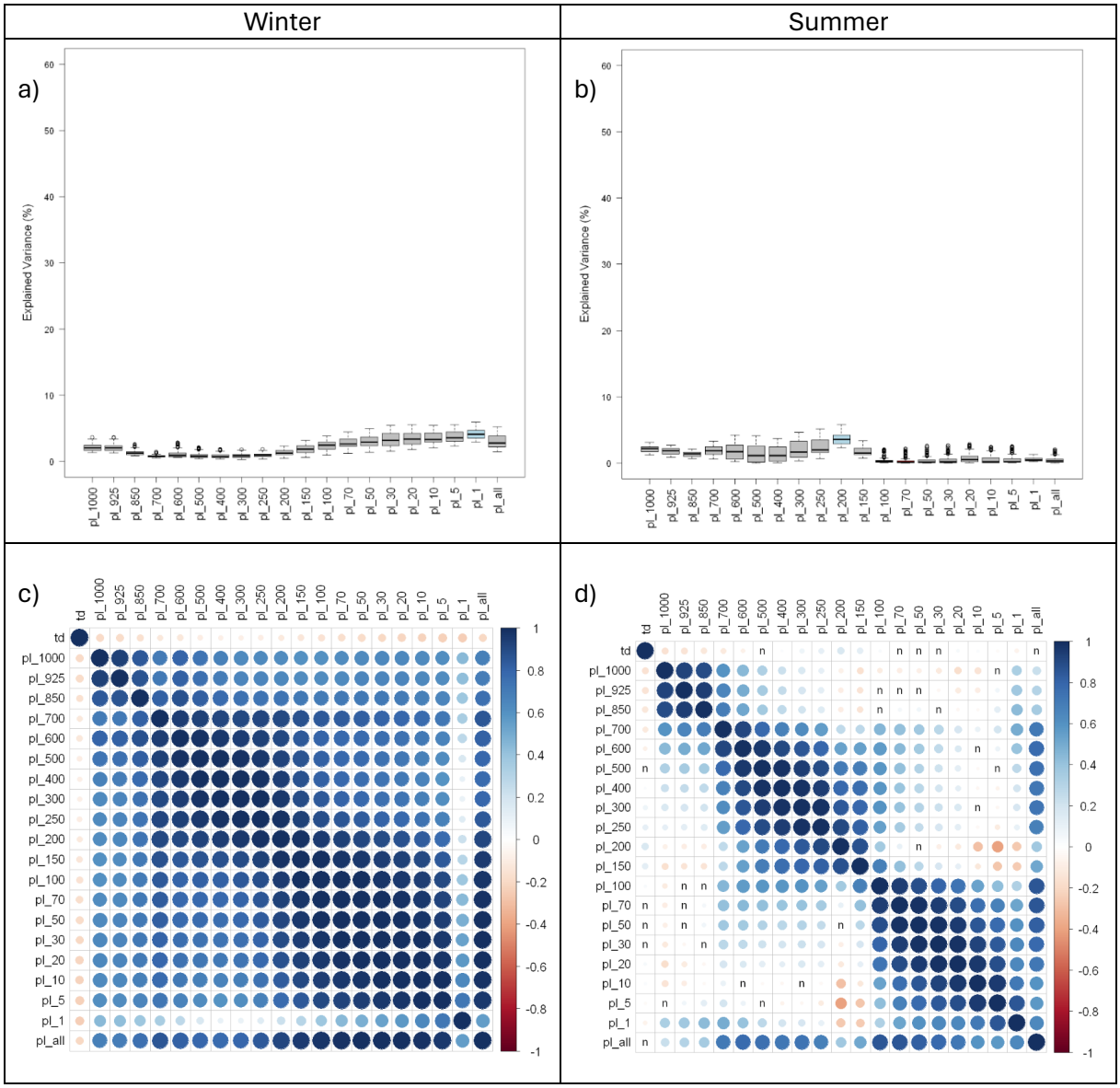

Fig. S2: Top row: explained variance in % for summer thaw depth (td) by eastward wind per hPa level over the Western Hemisphere. Blue and red are highest, respectively, lowest variance. a) Winter eastward wind (DJF), b) Summer eastward wind (JJA). Bottom row: Correlation of eastward wind on different pressure levels (in hPa) with summer thaw depth over Western Hemisphere. Direction of the correlation: blue is positive, red is negative. Strength of correlation is represented by the size of the circle. n in boxes stands for non-significant c) Winter (DJF) d) Summer (JJA).

8.3 Northward Wind in Eastern Hemisphere

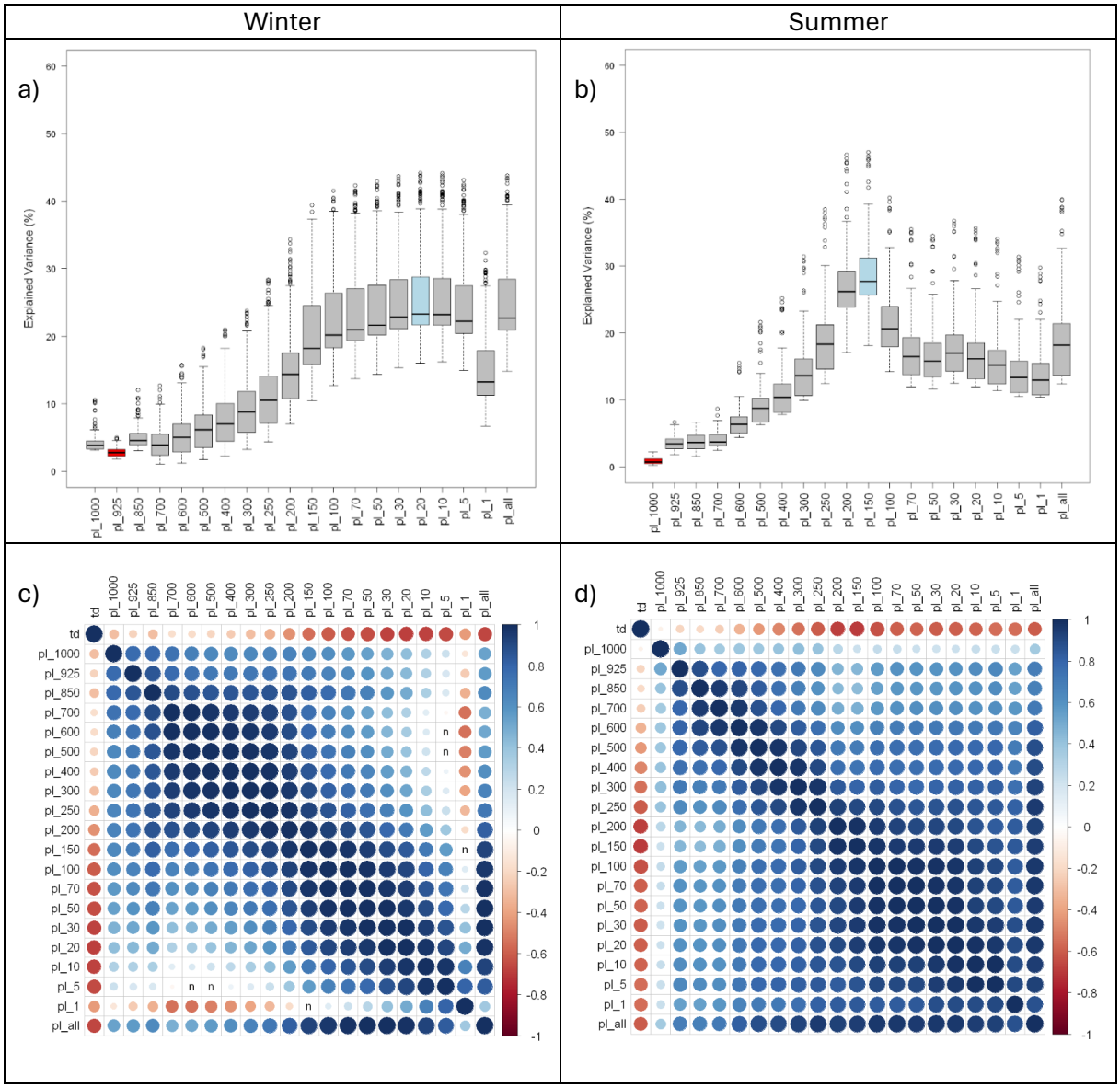

Fig. S3: Top row: explained variance in % for summer thaw depth (td) by northward wind per hPa level over the Eastern Hemisphere. Blue and red are highest, respectively, lowest variance. a) Winter northward wind (DJF), b) Summer northward wind (JJA). Bottom row: Correlation of northward wind on different pressure levels (in hPa) with summer thaw depth over Eastern Hemisphere. Direction of the correlation: blue is positive, red is negative. Strength of correlation is represented by the size of the circle. n in boxes stands for non-significant c) Winter (DJF) d) Summer (JJA).

8.4 Northward Wind in Western Hemisphere

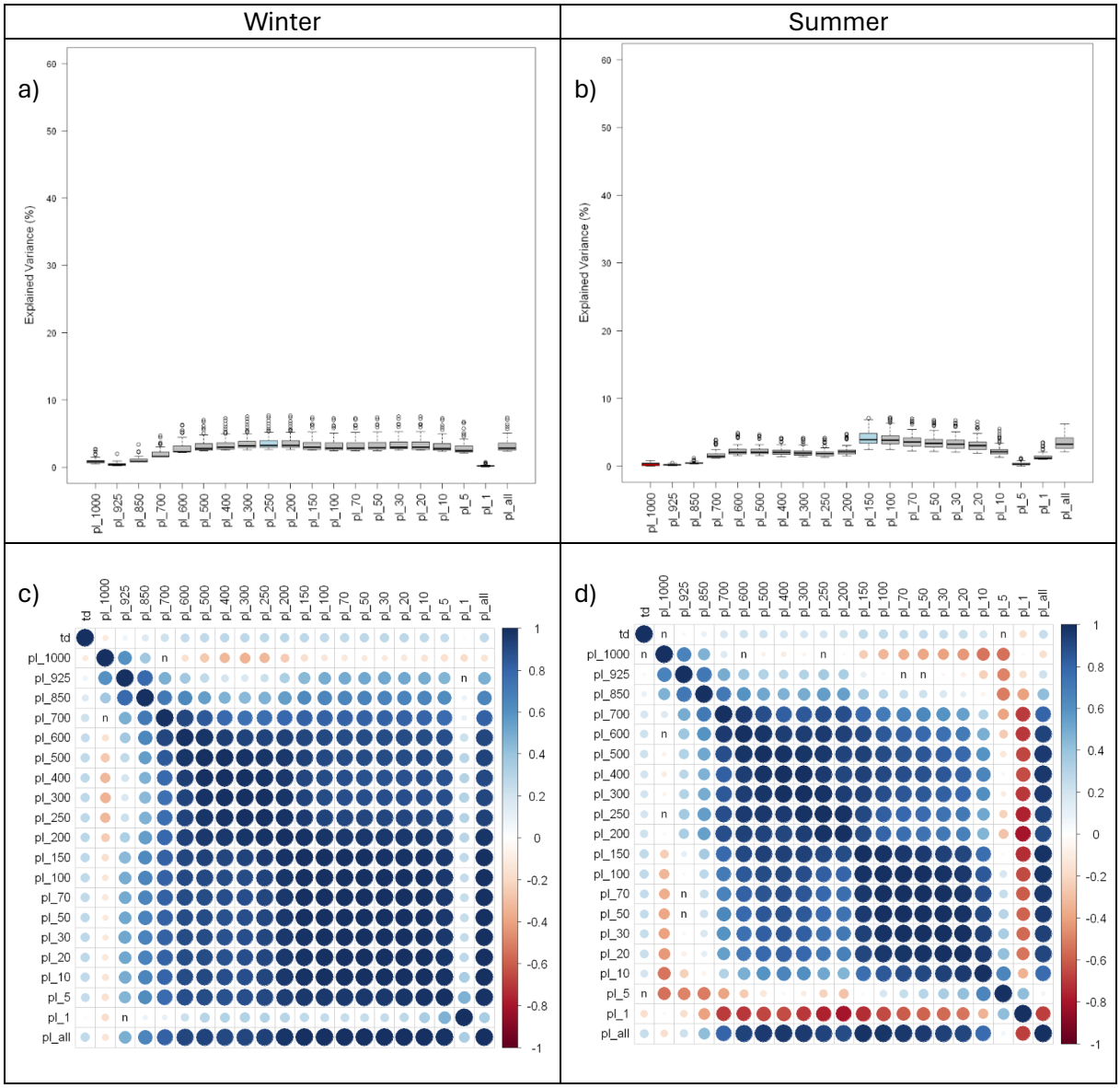

Fig. S4: Top row: explained variance in % for summer thaw depth (td) by northward wind per hPa level over the Western Hemisphere. Blue and red are highest, respectively, lowest variance. a) Winter northward wind (DJF), b) Summer northward wind (JJA). Bottom row: Correlation of northward wind on different pressure levels (in hPa) with summer thaw depth over Western Hemisphere. Direction of the correlation: blue is positive, red is negative. Strength of correlation is represented by the size of the circle. n in boxes stands for non-significant c) Winter (DJF) d) Summer (JJA).

8.5 Mass Fraction of Cloud Liquid Water in Eastern Hemisphere

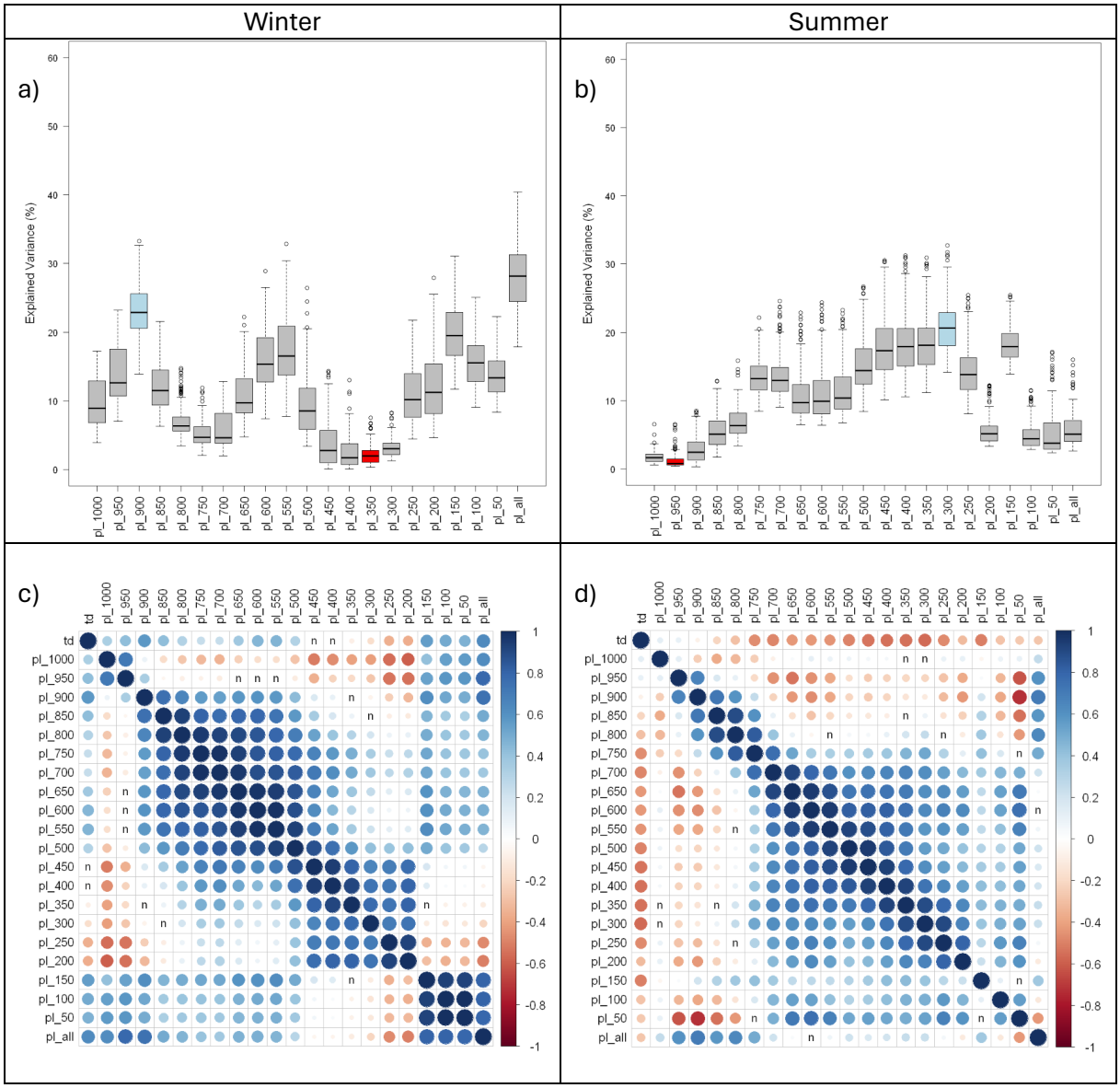

Fig. S5: Top row: explained variance in % for summer thaw depth (td) by mass fraction of cloud liquid water per hPa level over the Eastern Hemisphere. Blue and red are highest, respectively, lowest variance. a) Winter mass fraction of cloud liquid water (DJF), b) Summer mass fraction of cloud liquid water (JJA). Bottom row: Correlation of mass fraction of cloud liquid water at different pressure levels (in hPa) with summer thaw depth over Eastern Hemisphere. Direction of the correlation: blue is positive, red is negative. Strength of correlation is represented by the size of the circle. n in boxes stands for non-significant c) Winter (DJF) d) Summer (JJA).

8.6 Mass Fraction of Cloud Liquid Water in Western Hemisphere

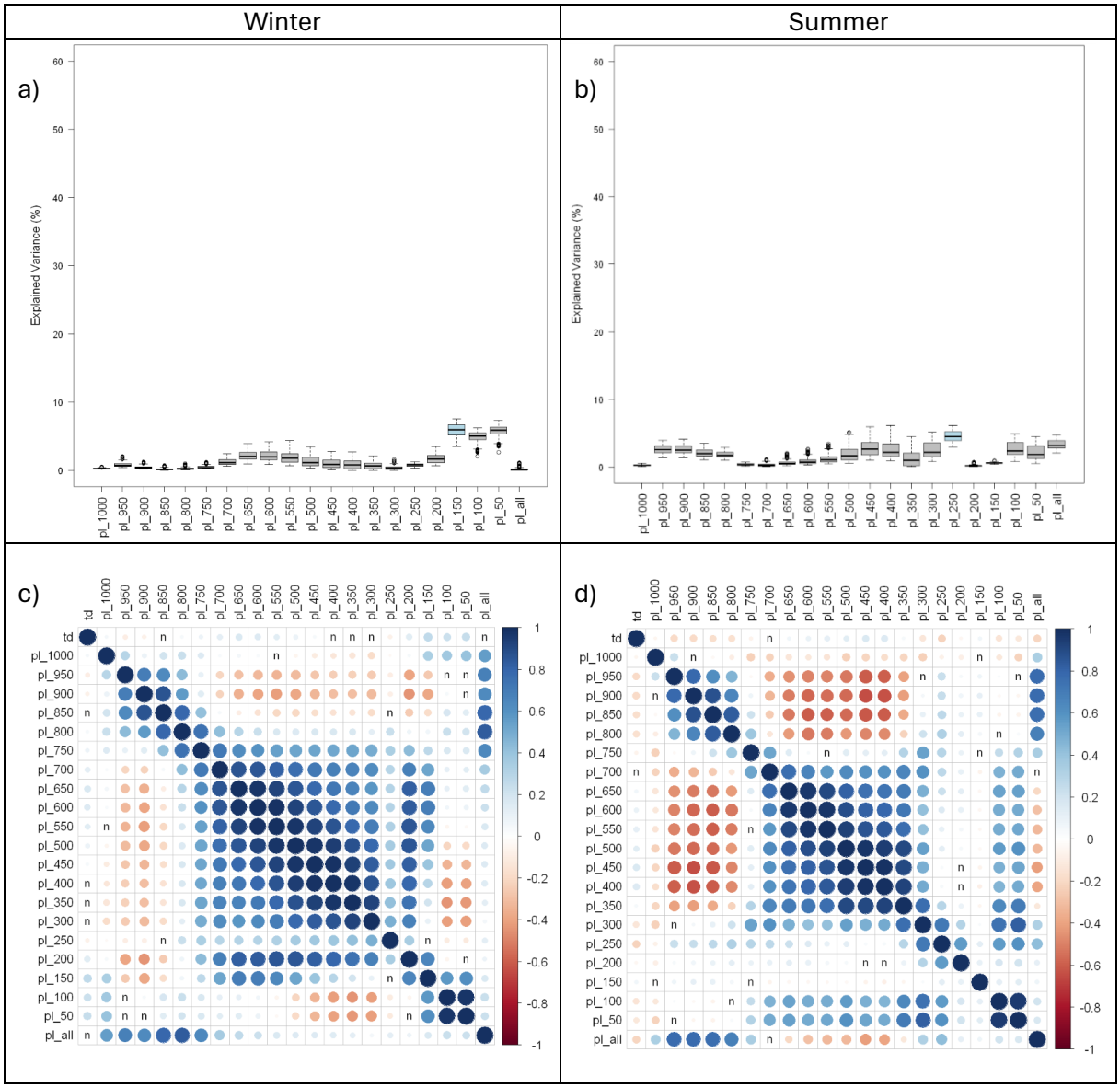

Fig. S6: Top row: explained variance in % for summer thaw depth (td) by mass fraction of cloud liquid water per hPa level over the Western Hemisphere. Blue and red are highest, respectively, lowest variance. a) Winter mass fraction of cloud liquid water (DJF), b) Summer mass fraction of cloud liquid water (JJA). Bottom row: Correlation of mass fraction of cloud liquid water at different pressure levels (in hPa) with summer thaw depth over Western Hemisphere. Direction of the correlation: blue is positive, red is negative. Strength of correlation is represented by the size of the circle. n in boxes stands for non-significant c) Winter (DJF) d) Summer (JJA).

8.7 Mass Fraction of Cloud Ice in Eastern Hemisphere

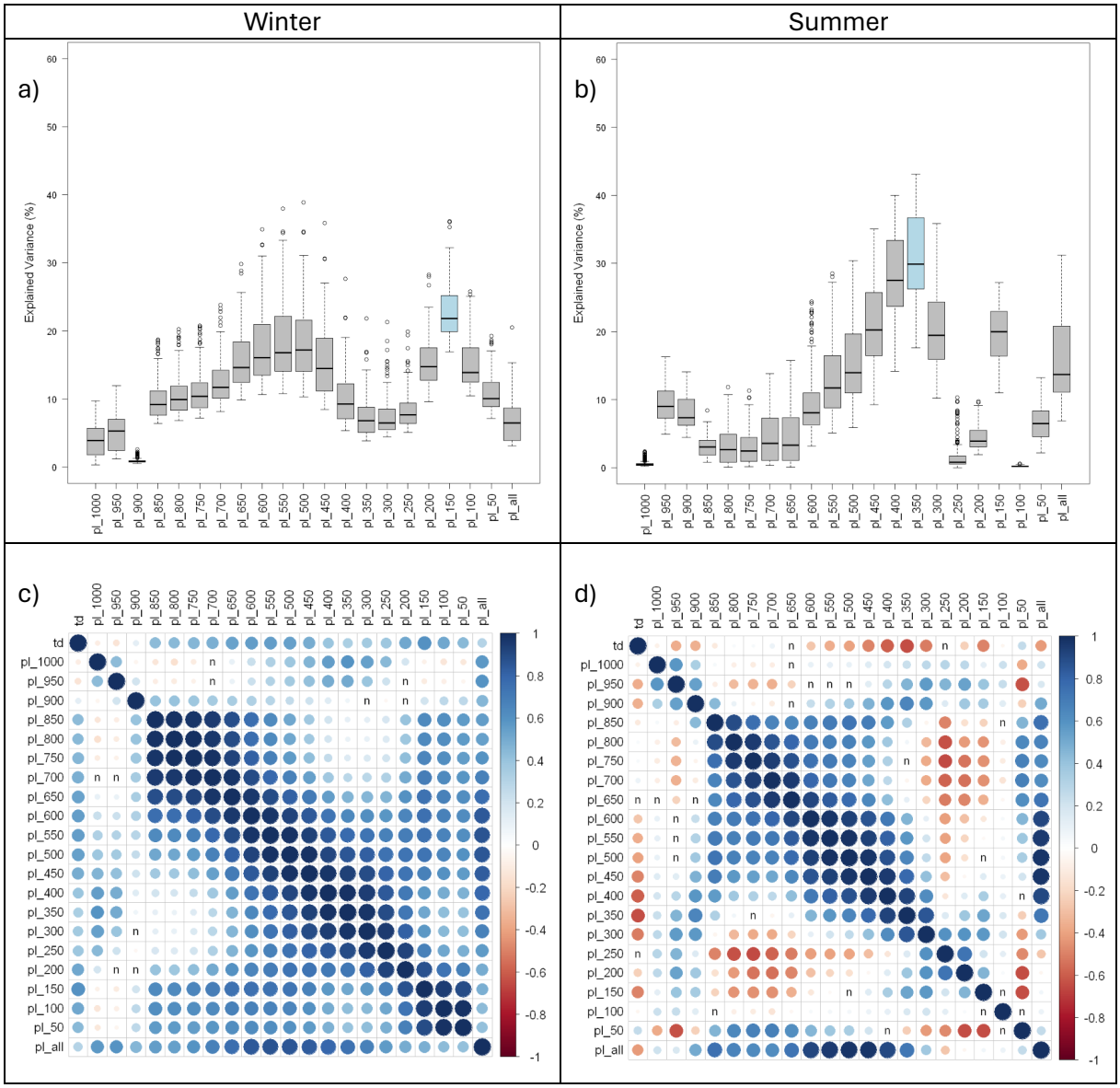

Fig. S7: Top row: explained variance in % for summer thaw depth (td) by mass fraction of cloud ice per hPa level over the Eastern Hemisphere. Blue and red are highest, respectively, lowest variance. a) Winter mass fraction of cloud ice (DJF), b) Summer mass fraction of cloud ice (JJA). Bottom row: Correlation of mass fraction of cloud ice at different pressure levels (in hPa) with summer thaw depth over Eastern Hemisphere. Direction of the correlation: blue is positive, red is negative. Strength of correlation is represented by the size of the circle. n in boxes stands for non-significant c) Winter (DJF) d) Summer (JJA).

8.8 Mass Fraction of Cloud Ice in Western Hemisphere

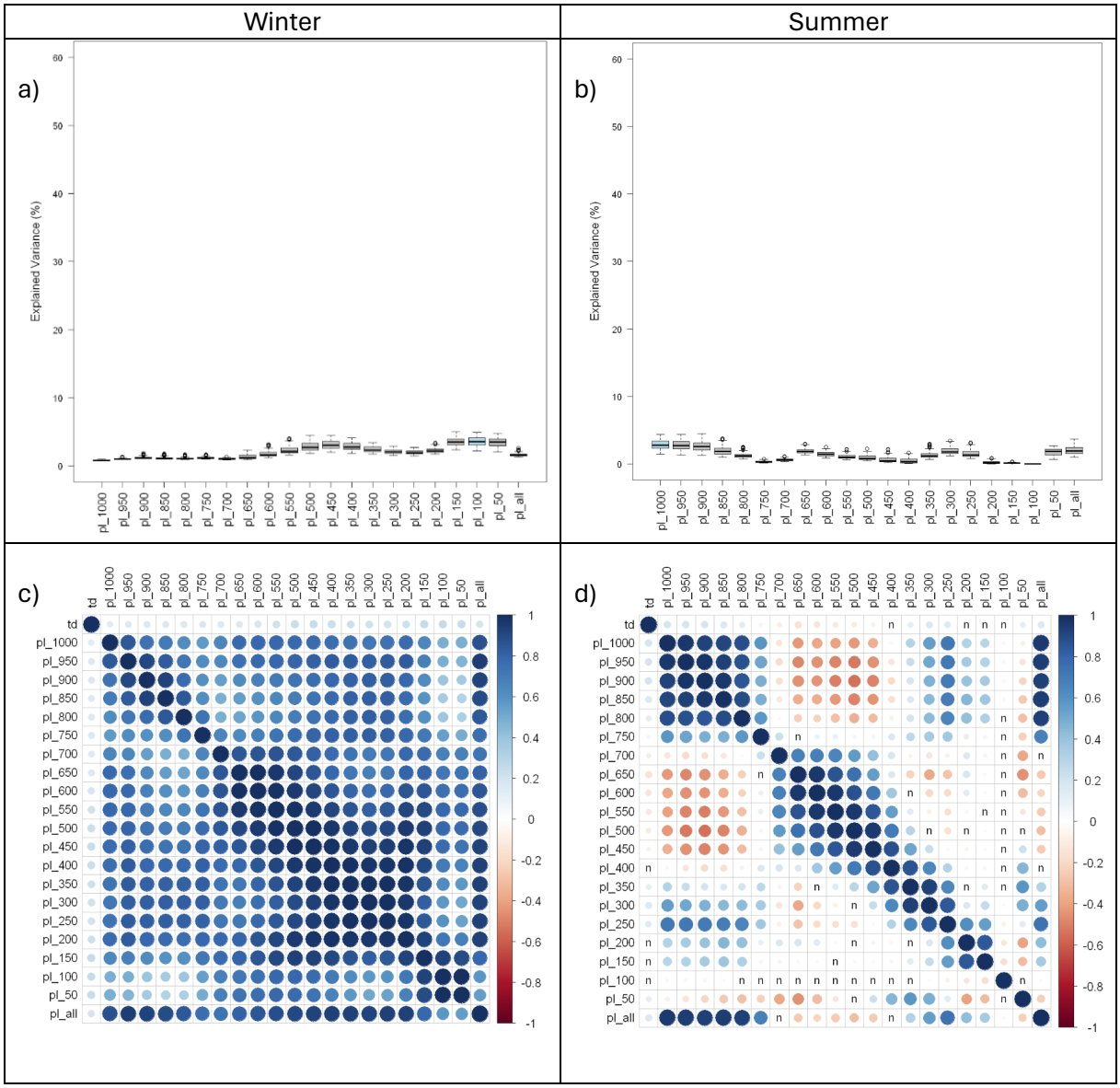

Fig. S8: Top row: explained variance in % for summer thaw depth (td) by mass fraction of cloud ice per hPa level over the Western Hemisphere. Blue and red are highest, respectively, lowest variance. a) Winter mass fraction of cloud ice (DJF), b) Summer mass fraction of cloud ice (JJA). Bottom row: Correlation of mass fraction of cloud ice at different pressure levels (in hPa) with summer thaw depth over Western Hemisphere. Direction of the correlation: blue is positive, red is negative. Strength of correlation is represented by the size of the circle. n in boxes stands for non-significant c) Winter (DJF) d) Summer (JJA).

8.9 Explained Variance and Correlation for Summer Thaw Depth in Eastern Hemisphere, G6solar-ssp245

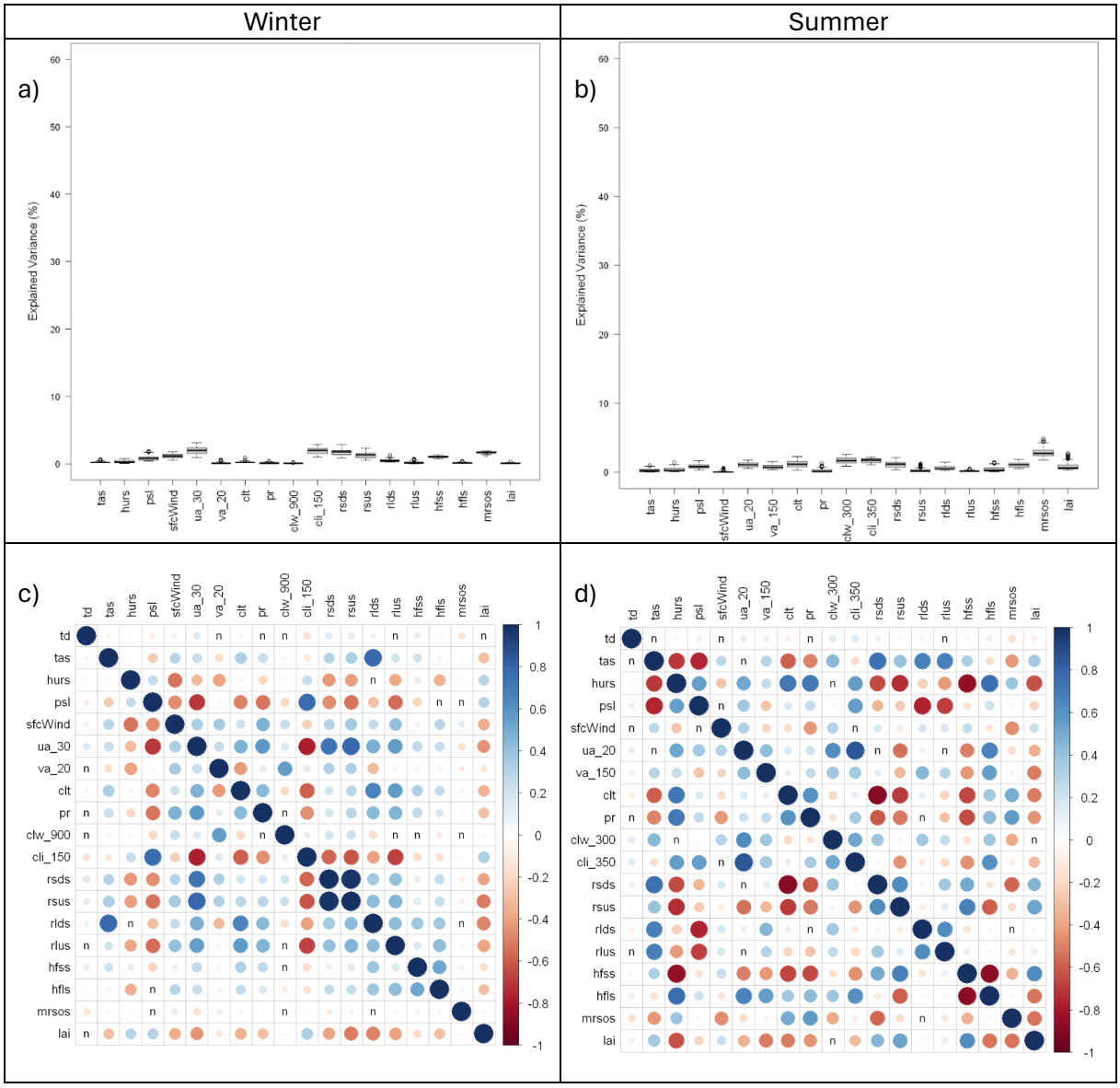

Fig. S9: Top row: explained variance (%) for summer thaw depth (td) per predictor and season over the Eastern Hemisphere for the difference G6solar versus ssp245. Predictors include: tas (air temperature), hurs (relative humidity), psl (air pressure at sea level), sfcWind (surface wind speed), ua (zonal northward wind at indicated hPa level), va (zonal northward wind at indicated hPa level), clt (cloud cover), pr (precipitation), clw (mass fraction cloud liquid water at indicated hPa level), cli (mass fraction of cloud liquid ice at indicated hPa level), rsds (radiation shortwave downwelling surface), rdus (radiation shortwave upwelling surface), rlds (radiation longwave downwelling surface), rlus (radiation longwave upwelling surface), hfss (sensible heat flux), hfls (latent heat flux), mrsos (moisture in the upper portion of the soil column), lai (leaf area index). a) Drivers from the winter season (DJF) b) Drivers from the summer season (JJA). Bottom row, Correlation matrix of the drivers per season. The direction of the correlation is indicated by the color, blue for positive correlation, red for negative correlation. The size of the circle represents the strength of the correlation. 'n' in boxes indicates non-significant correlation. c) Winter season (DJF) d) Summer season (JJA).

8.10 Explained Variance and Correlation for Summer Thaw Depth in Western Hemisphere, G6solar-ssp245

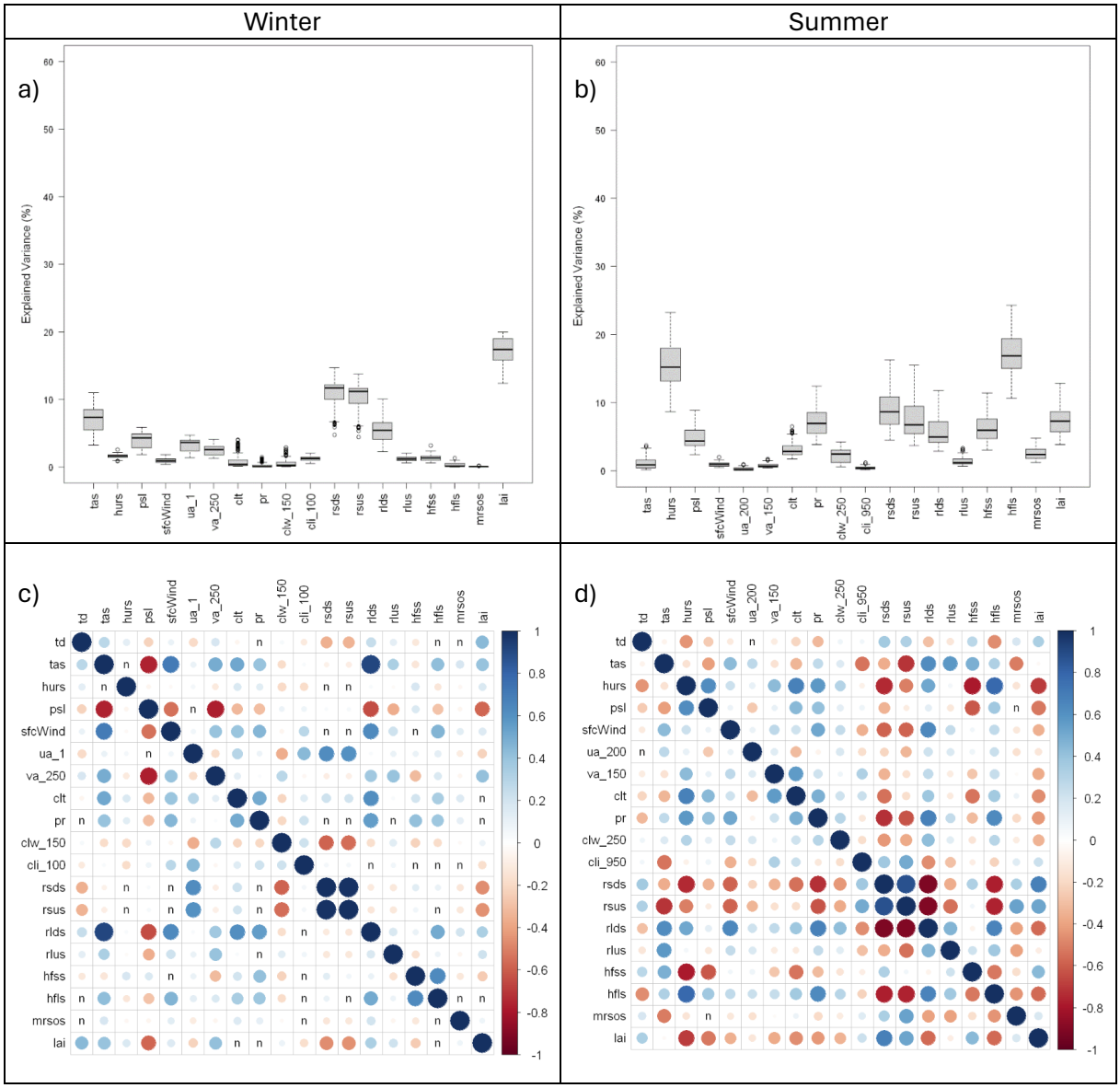

Fig. S10: Top row: explained variance (%) for summer thaw depth (td) per predictor and season over the Western Hemisphere for the difference G6solar versus ssp245. Predictors include: tas (air temperature), hurs (relative humidity), psl (air pressure at sea level), sfcWind (surface wind speed), ua (zonal northward wind at indicated hPa level), va (zonal northward wind at indicated hPa level), clt (cloud cover), pr (precipitation), clw (mass fraction cloud liquid water at indicated hPa level), cli (mass fraction of cloud liquid ice at indicated hPa level), rsds (radiation shortwave downwelling surface), rdus (radiation shortwave upwelling surface), rlds (radiation longwave downwelling surface), rlus (radiation longwave upwelling surface), hfss (sensible heat flux), hfls (latent heat flux), mrsos (moisture in the upper portion of the soil column), lai (leaf area index). a) Drivers from the winter season (DJF) b) Drivers from the summer season (JJA). Bottom row, Correlation matrix of the drivers per season. The direction of the correlation is indicated by the color, blue for positive correlation, red for negative correlation. The size of the circle represents the strength of the correlation. 'n' in boxes indicates non-significant correlation. c) Winter season (DJF) d) Summer season (JJA).

8.11 Zonal Wind in Troposphere

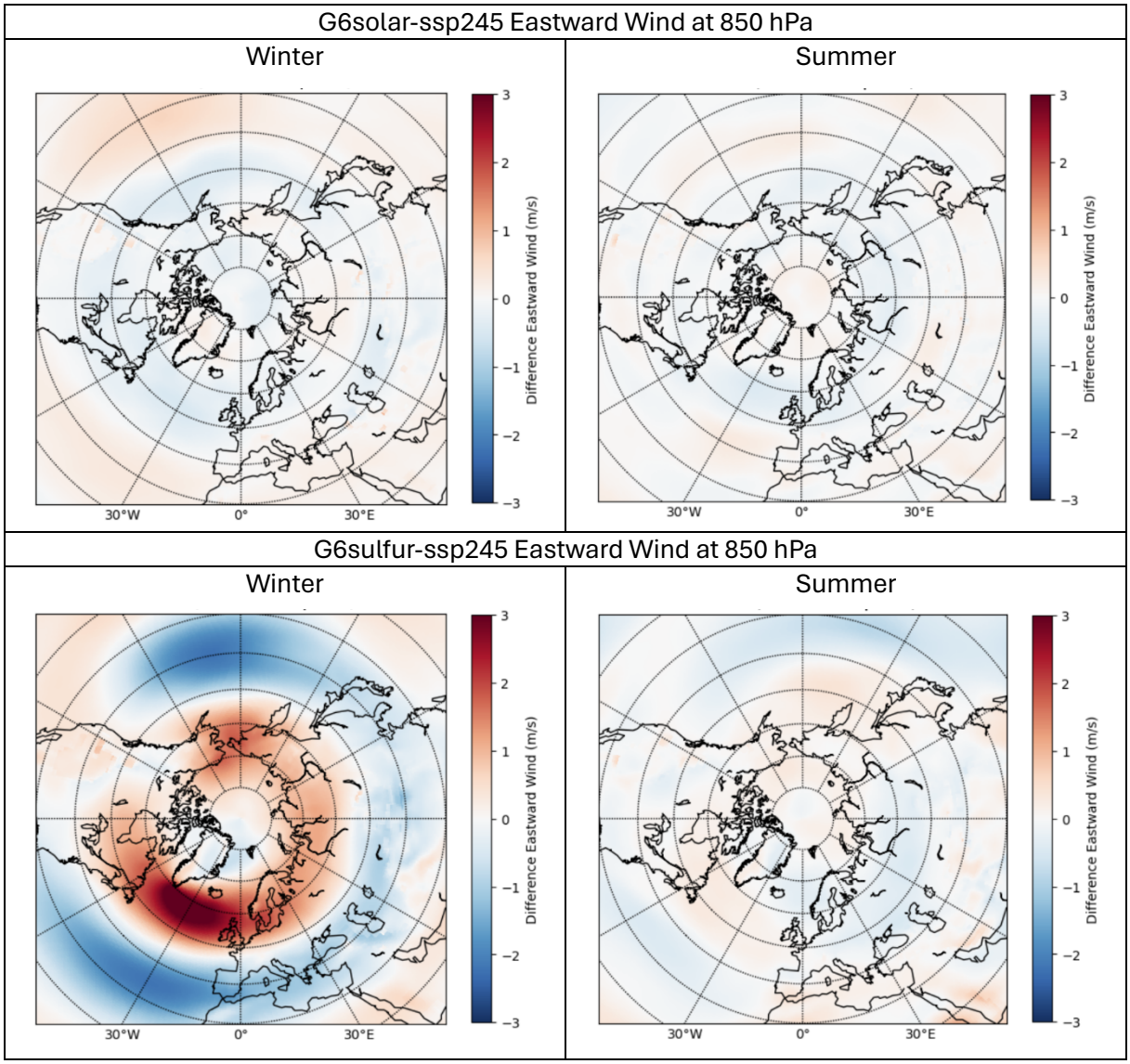

Fig. S11: Difference in Eastward Wind (m/s) at the 850 hPa level. Winter (DJF), Summer (JJA). Top row: G6solar-ssp245, bottom row: G6sulfur-ssp245.

8.12 Zonal Wind in Stratosphere

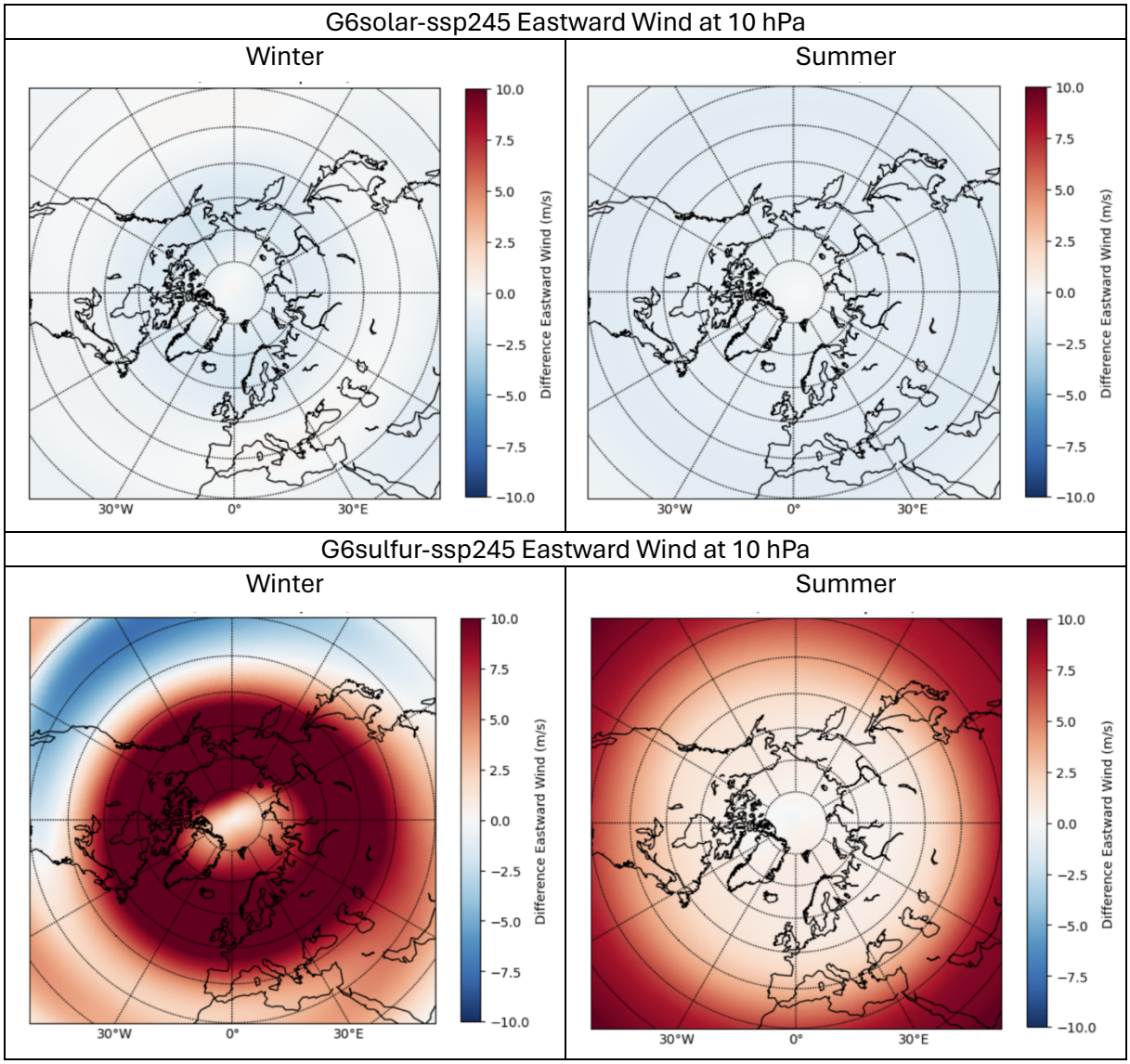

Fig. S12: Difference in Eastward Wind (m/s) at the 10 hPa level. Winter (DJF), Summer (JJA). Top row: G6solar-ssp245, bottom row: G6sulfur-ssp245.

8.13 Meridional Wind in Troposphere

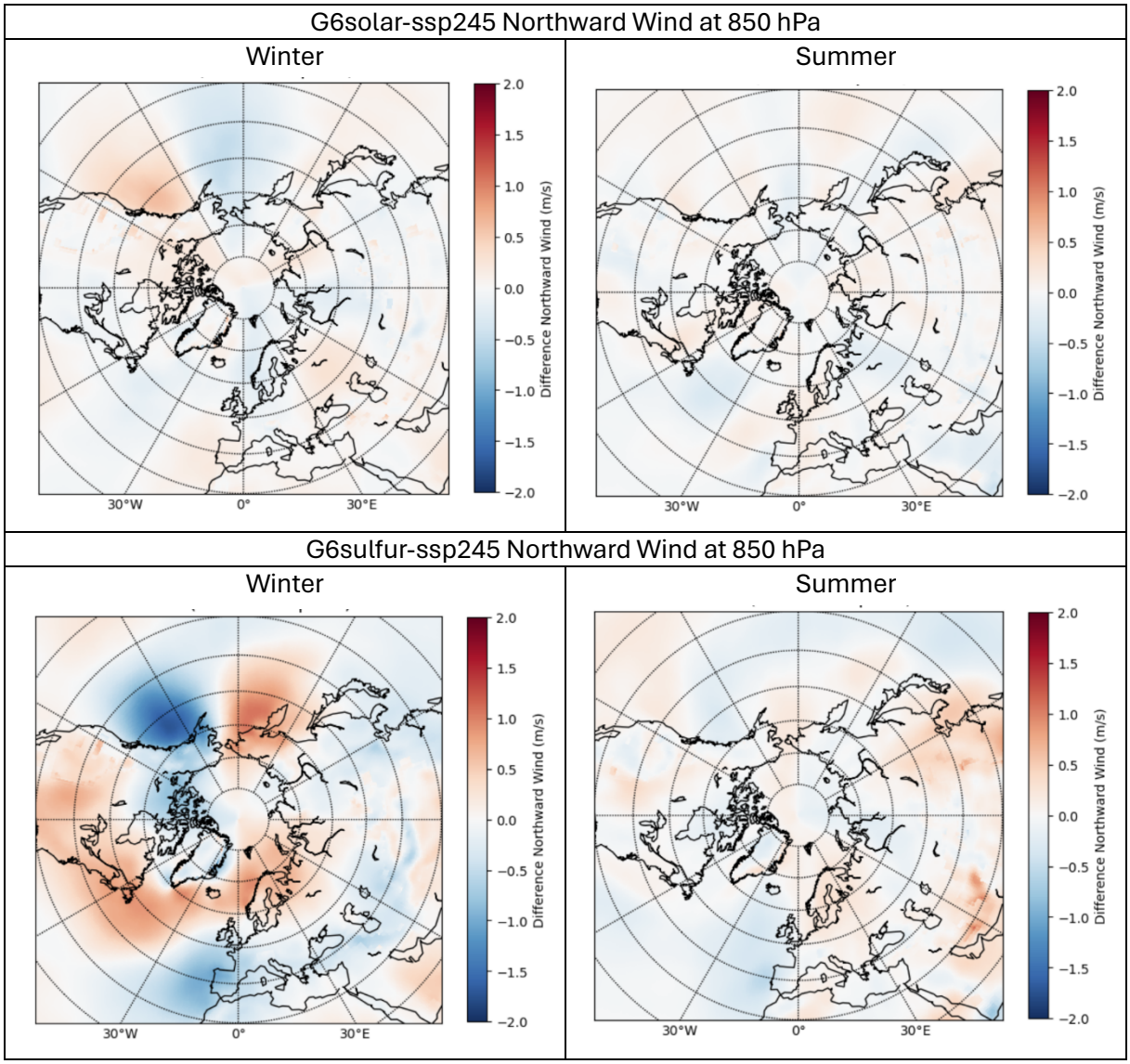

Fig. S13: Difference in Northward Wind (m/s) at the 850 hPa level. Winter (DJF), Summer (JJA). Top row: G6solar-ssp245, bottom row: G6sulfur-ssp245.

8.14 Meridional Wind in Stratosphere

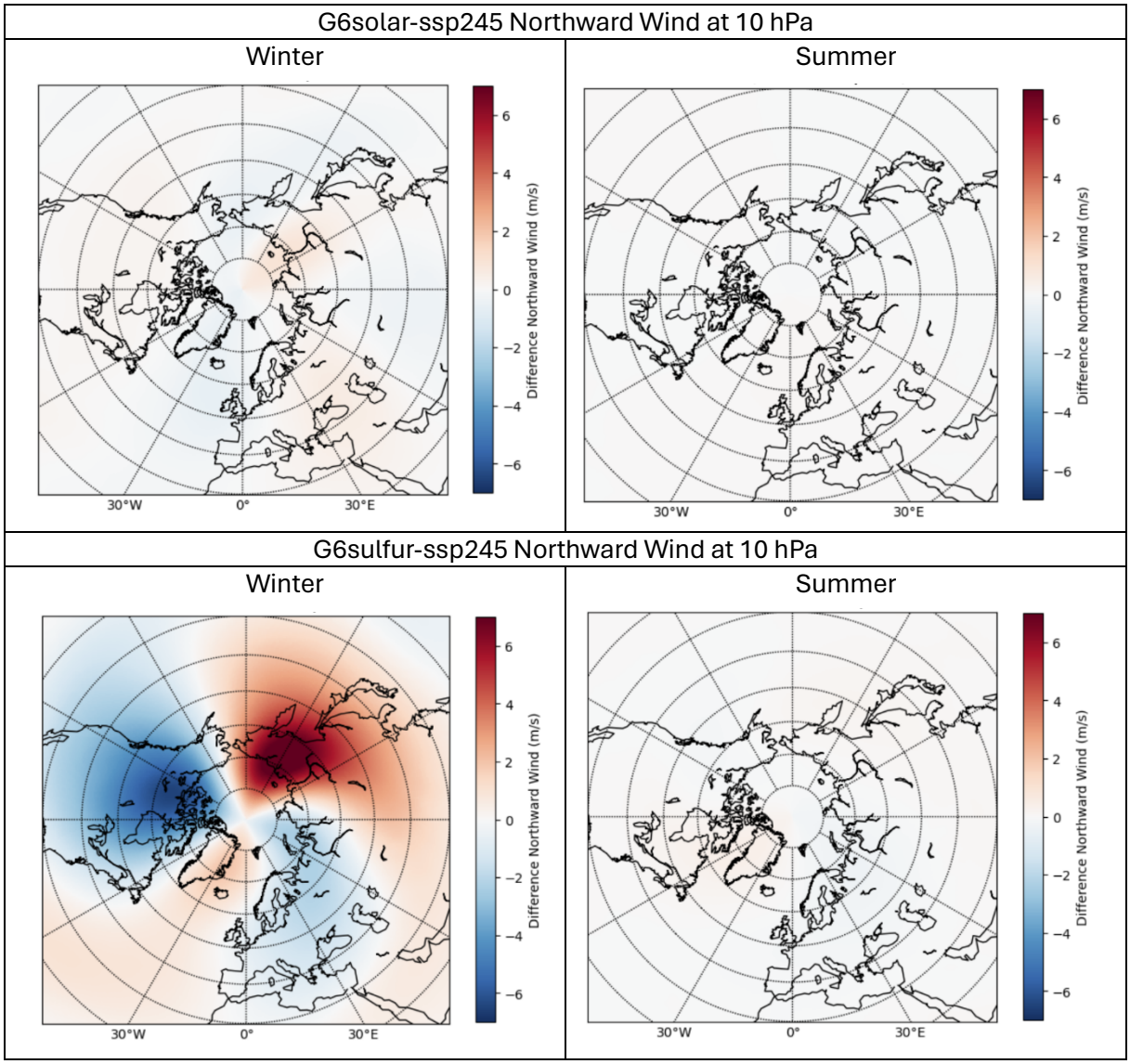

Fig. S14: Difference in Northward Wind (m/s) at the 10 hPa level. Winter (DJF), Summer (JJA). Top row: G6solar-ssp245, bottom row: G6sulfur-ssp245.

Personal declaration

Personal declaration: I hereby declare that the submitted thesis is the result of my own, independent work. All external sources are explicitly acknowledged in the thesis.

Zurich, 30 April 2024

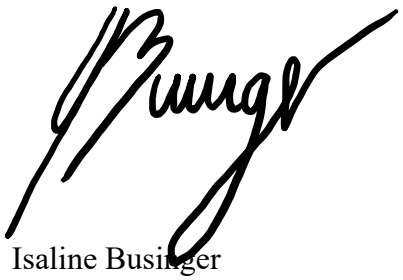

Isaline Businger